Immune-mediated inflammation modulates the thalamostriatal circuitry regulating depression-like behaviour in both mice and humans

Deepika Sharma[1, +], Lilya Andrianova[1,2, +], Rhona McGonigal[1, +], Kirstyn Gardner-Stephen[1], Hassan al Fadhel[1], Flavia Sunzini[1], Kristian Stefanov[1], Jennifer A Barrie[1], Richard Hohne[1], Megan Saathoff[1,3], Yaprak Karabalci[2], Alfredo Montes Gomez[1], Julie-Myrtille Bourgognon[1,2], Peter Thornton[3], Neil Basu[1], John J Cole[4], Michael T Craig[2, *], Jonathan T Cavanagh[1, *]

[+]contributed equally

*corresponding author

[1] School of Infection & Immunity, College of Medical, Veterinary & Life Sciences, Sir Graham Davies Building, University of Glasgow, Glasgow G12 8QQ. UK

[2] School of Psychology & Neuroscience, College of Medical, Veterinary & Life Sciences, Sir James Black Building, University of Glasgow, Glasgow G12 8QQ. UK

[3] NodThera, NodThera, Suite 8, The Mansion, Chesterford Research Park, Cambridge, CB10 1XL, UK

[4] Molecular Analysis, MVLS Shared Research Facilities, College of Medical, Veterinary & Life Sciences, Joseph Black Building, University of Glasgow, Glasgow G12 8QQ. UK.

Correspondence to Jonathan.cavanagh@glasgow.ac.uk or mick.craig@glasgow.ac.uk

Keywords: Synaptic transmission, Anhedonia, Depression, Neuroinflammation, T cell biology, Glia, Thalamus, Striatum, Neurobiology, Immunology

Abstract

Major depressive disorder (MDD) affects 3.8% of the world population, representing a significant contribution to the global burden of disease (WHO). Around a quarter of people living with MDD demonstrate low-grade inflammation and substantial evidence links peripheral inflammation to anhedonia via disrupted cortico-thalamo-striatal circuitry. We examined clinical human neuroimaging in individuals with systemic inflammation (psoriatic disease), and employed a preclinical model of neuroinflammation, to study relationships between the neuroinflammatory response, neural circuitry and depression-like behaviours. Our preclinical model used a topical treatment of Aldara®, which contains imiquimod (a TLR7/8 agonist) that also induces a psoriasis-like phenotype. Changes in functional connectivity between thalamus and ventral striatum correlated with depression in humans with psoriatic disease, and with anhedonia-like behaviours in Aldara-treated mice. Mice treated with Aldara exhibited reduced sucrose preference and impairments in intrinsic motivational behaviours relative to untreated controls. Within 4 to 6 hours of Aldara treatment, neurons in midline thalamus were activated substantially more than in control animals. Optogenetic activation of midline thalamic projections onto ventral striatum medium spiny neurons revealed that repeated Aldara treatment substantially reduced the magnitude of the evoked thalamic AMPA receptor-mediated post-synaptic currents. In the preclinical model, contributions from both resident and infiltrating immune cells drove neuroinflammation. Further dissection of these pathways revealed that NLRP3 inflammasome activation, infiltrating monocytes and infiltrating T cells all contributed to the neuroinflammatory effects of Aldara.

Introduction

Growing evidence implicates neuroinflammation in the pathophysiology of depression and other neuropsychiatric disorders. Notably, up to 75% of patients with immune-mediated inflammatory disease (IMIDs) such as psoriatic disease experience comorbid depression[1,2], underscoring the important influence of immune activity on mental health. Treatment with immune therapies that target key inflammatory molecules also alleviate the comorbid depression in IMIDs for some, but not all, patients[3], and a recent meta-analysis found that elevated markers of peripheral inflammation may predict resistance to anti-depressant treatment[4]. The behavioural consequences of neuroinflammation in humans include a negative impact on mood/reward responses, anxiety, energy levels and cognition, but targeted therapies remain elusive.

A recent large-scale genome-wide association study (GWAS) implicated the gene *TRAF3* in major depressive disorder (MDD)[5]. This gene encodes a protein that is key to the interferon-driven immune response, and individuals treated with interferon-α (IFN-α) are at heightened risk of developing depression[6]. Meta-analyses of multiple GWAS studies have also implicated immune-related genes in MDD[7]. Human brain imaging reveals that IFN-α treatment rapidly reduced global connectivity within the brain, and local changes in connectivity between striatum and cortex[8]. Subsequent work found that treatment with IFN-α and anti-TNFα (tumour necrosis factor-α) had opposing effects on depressive symptoms, and resulted in consistent changes in brain connectivity[9,10].

While human studies can reveal correlative associations between brain activity, inflammation and MDD, understanding the neurobiological changes that occur in neural circuits in response to inflammation requires animal models to allow determination of mechanistic insights and causal inferences. Chronic mild stress in rats drives anhedonic behaviour and is associated with increased TNFα and IL-1β in hypothalamus[11], and lipopolysaccharide (LPS) administration is also widely used to model inflammation-mediated depression in rodents[12]. Treatment with poly (I:C) in mice results in monocyte infiltration to the brain with consequent impaired motor learning and learning-related dendritic spine plasticity through TNFα-dependent mechanisms[13]. TNFα plays an important role in

homeostatic control of glutamatergic neurotransmission, with astrocyte-derived TNFα required both for scaling of synaptic strength[14] and astrocytic glutamate cycling[15]. But excessive TNFα can be maladaptive, with intracerebroventricular infusion of TNFα sufficient to perturb striatal glutamatergic neurotransmission in a manner similar to that observed in experimental autoimmune encephalopathy[16]. Application of TNFα to brain slices evokes region-specific changes in synaptic function, reducing the AMPA/NMDA ratio in striatum but increasing it in hippocampus[17]. TNFα acts directly on TNFR1 receptors on neurons to alter AMPA and GABA receptor trafficking within minutes of TNFα application in culture[18]. Together, these data show that cytokines such as TNFα can influence glutamatergic transmission via both neuronal and astrocytic mechanisms.

The neurobiological mechanisms through which neuroinflammation can drive depression and anhedonia in humans remain unclear. Cellular sources of cytokines in the brain include both resident and recruited cells. For example, a specific pathway involving activation of the NLPR3 inflammasome in reactive microglia can lead to activated neurotoxic astrocytes[19]. Depression-like behaviours can also be observed in well-validated rodent inflammation models, affording an opportunity to explore these mechanisms. Here, we sought to characterise the molecular and cellular changes occurring in the brain during neuroinflammation, and how these affect the neural circuitry of motivation. Typically, animal models of neuroinflammation use acute peripheral stimuli that drive a strong immune response. It is unclear whether these acute immune activations drive similar or distinct mechanisms from the low-level chronic immune activation seen in humans with inflammation-associated depression. We therefore used a TLR7/8 agonist (Aldara®; active ingredient 5% Imiquimod [IMQ]) that directly accesses the brain and provides a non-invasive sub-chronic model of psoriasis and neuroinflammation, with the peripheral and central inflammatory responses reported in our previous work[20,21]. We found neuroinflammation in this model was driven by both reactive glia and infiltrating peripheral immune cells, leading to changes in thalamostriatal function and anhedonia-like behaviour in mice. We also analysed human brain imaging data in individuals with psoriatic disease, and found that connectivity between thalamus and ventral striatum positively correlated with depression score,

suggesting that neurobiological mechanisms of inflammation-driven affective change may be similar in the preclinical model and in humans.

Material and Methods

Mice

Female C57BL/6J mice were obtained from Charles River Laboratories (UK) and housed in individual ventilated cages. Animals underwent acclimatisation for one week prior to experimental use at 8 to 10 weeks of age (group numbers are described per experiment below). Animals were maintained in a 12 h light/dark cycle in controlled temperature and humidity with *ad libitum* access to food and water. All experiments were carried out in accordance with the UK Animal (Scientific Procedures) Act 1986 and were subject to local ethical approval by the University of Glasgow Animal Welfare and Ethical Review Board. The iCCR$^{-/-}$ mice, with genes deleted for four inflammatory chemokine receptors *CCR1, CCR2, CCR3 and CCR5 (iCCRs),* were obtained from the Chemokine Research Group within the University. These animal strains were generated and maintained on a C57BL/6 background and bred in a specific pathogen-free environment.

Aldara model

C57BL/6, and iCCR$^{-/-}$ female mice (8 to 22 weeks old, starting weight range: 16.3 – 29.5 g) were each treated with a ~62.5 mg dose of Aldara™ (Meda AB, UK) cream containing 5% Imiquimod - IMQ or an equivalent volume of control cream (Boots Aqueous Cream B.P.; Boots Pharmacy, UK) by topical application to shaved dorsal skin near the base of the tail (~3 mm^2 area). Treatment was applied for 3 consecutive days, with tissue collected 24h after the final application. Soft diet was provided to both control and experimental groups and mice monitored daily for weight loss. Female mice only were used in this study due to male mice showing differences in inflammatory response to topical application of inflammatory agents[21].

Experimental design

Mice were randomly allocated to treatment groups. A power analysis was performed using G*Power [22] software (v3.0.10 G*Power, RRID:SCR_013726) to determine minimum group size; n = 4/5 (immunostaining), n = 4 (flow) and n = 8 (behaviour) were selected for each treatment group. The effect size for output was based on previous or pilot experiments, with calculations made on a basis of 80% power, and a significance criterion of 0.05. All tissue was coded prior to imaging and analysis to prevent researcher bias.

Behavioural assessment

Animals

Following acclimatisation, they were singly housed in rat cages (previously washed and sterilised to eliminate any other species' scents), equipped with a running wheel and two water bottles, one of which contained 0.1% (w/v) sucrose solution, available *ad libitum*, to which the mice were acclimatised. Behavioural testing was conducted throughout (nest-building, sucrose preference) or on day 4, 24 hours after the last application of cream. Elevated plus maze was conducted in the morning and mice were returned to their cage room for 2 – 3 hours before performing open field test in the afternoon. Before each test, mice were allowed to acclimatise to the behaviour room for 30 mins prior to the start of testing.

Sucrose preference

Mice were allowed to establish their pattern of consumption of water and sucrose over the course of several days, prior to the treatment with topical creams. Both water bottles were weighed in the mornings and evenings and the change in weight was compared as a ratio of sucrose preference.

Nest building

We used the Deacon nest-building protocol[23]. Pressed unbleached cotton squares of 3 g (± 0.05 g) each were given every morning for nest building and collected the following morning. The images of the nests were taken for rating out of 5 (where 5 points were given to a fully shredded cotton material

built up into a high walled nest, covering the mouse; 1 point reflects an untouched pressed cotton material) in the evenings as well as following mornings. The non-shredded material was weighed as another measure of nest building.

Elevated plus maze

To assess anxiety, mice were placed into cross shaped Perspex arena (110 cm x 110 cm, 65 cm from ground) for one trial of 5 mins only and recorded using ANY-maze video-tracking software (ANY-maze, Ireland). ANY-maze software was also used to analyse the following: distance travelled, average and maximal speed in different parts of the arena (closed arms *vs* open arms) as well as numbers of entries and time spent in open arms (OA) versus closed arms (CA) of the arena.

Open field test

To assess locomotor activity and as a secondary measure of anxiety in a novel arena environment, mice were placed into individual Perspex boxes (40 x 40 x 45 cm) for 1 h and recorded using ANY-maze video-tracking software. First 15 mins were analysed using ANY-maze software, and measures recorded included distance travelled, average and maximal speed in different parts of the arena as well as numbers of entry and time spent in centre and perimeter of the arena.

Rotarod

We measured locomotor activity using an ITC Rotarod (IITC Life Sciences Inc, USA). Mice were habituated to the room for 30 min prior to testing, and acclimatised to the accelerating rotarod (0 – 60 rpm) for 3 trial runs the day before recording. A baseline performance was recorded immediately before the first topical cream application. Mice were placed on the beam in separate lanes of the rotarod apparatus. Latency to fall from the rod was recorded for up to 300 s each trial for three trials per day on 3 consecutive days. The latency to fall compared to the baseline was reported per mouse and compared between groups.

Human neuroimaging

As part of an observational study with patients living with an immune-mediated inflammatory disease (psoriatic disease, PsD), we used 3T MRI to characterize the thalamo-striatal connectivity association with depression. The PsD clinical cohort (n=46) had a mean age of 49 years (SD 11.2), was 52% female, and demonstrated high to moderate disease activity (mean Disease Activity in Psoriatic Arthritis [DAPSA] 40.8, SD 19) with an average disease duration of 6.4 years (SD 5.8). Depressive symptoms were assessed using the standardised PROMIS Depression short form: 68% met criteria for depressive symptoms, including 13% classified as severe, 15% moderate, and 30% mild (see supplementary table 1).

We defined bilateral nucleus accumbens and thalamus based on the Harvard-Oxford Atlas. Functional connectivity (FC) was calculated as Fisher z transformed Pearson correlation coefficients between the time series of BOLD signal changes between bilateral thalamus and bilateral nucleus accumbens after preprocessing using the default CONN toolbox pipeline[24] . Linear regression was used to demonstrate an association between thalamocortical connectivity and depression in PsD, after controlling for age and sex.

We computed brain maps of amplitude of low-frequency fluctuations (ALFF) in the CONN toolbox to determine the baseline activity in thalamostriatal regions in relation to depression. These maps represent a measure of BOLD signal power within the frequency band (0.008–0.09 Hz) and are defined as the root mean square of BOLD signal at each individual voxel[25]. ALFF values were normalised for each patient, thus the distribution of ALFF values across all voxels is normal. This allows the normalised ALFF values to show the relative amplitude compared to other areas: positive values indicating more active compared to average activity, negative values indicating less active. These ALFF values were then used in linear regressions with depression scores after controlling for age and sex to determine any association between thalamostriatal activity and depression in PsA.

Ethical approval was granted by the West of Scotland Research Ethics Committee (ref 19/WS/0033), and all participants provided written informed consent in accordance with the Declaration of Helsinki. The study was funded by Versus Arthritis (grant ref: 21964).

Stereotaxic surgeries

Several midline thalamic nuclei target ventral striatum including but not limited to paraventricular (PVT), centromedian (CM) and parataenial (PT) thalamic nuclei[26]. To broadly target midline thalamus for optogenetic and electrophysiological experiments, we carried out stereotaxic injections to deliver 300 nl of AAV8-hSyn-Chronos-GFP (UNC Viral Vector Core, USA; contributed by Ed Boyden; titre 3.1×10^{13} viral particles / ml) to the border of CM and PVT. We used the following stereotaxic coordinates: R/C -0.5 mm and M/L 0 mm from Bregma, at a depth of 3.3 mm from the pial surface. Briefly, mice were anaesthetised with 5% Isoflurane, were placed on a heated pad for the duration of the surgery and maintained at 1.5–2.5% isoflurane (with a flow rate of ~2 l min^{-1} O_2). Mice were then subcutaneously dosed with 0.1 mg/kg of buprenorphine (buprenorphine hydrochloride, Henry Schein) and 5 mg/kg of carprofen (Rimadyl, Henry Schein) at the start of surgery, and additional doses of carprofen were provided subcutaneously subsequent days, as required. Anaesthetised mice were placed in a Kopf 940 Small Animal stereotaxic frame (David Kopf Instruments, CA, USA). An incision was made down the midline, and a craniotomy was performed to allow injection of virus (300 nl) using a Neuros Syringe (Hamilton Company, NV, USA) injected at a rate of 100 nl/min using a UMP3 UltraMicroPump (World Precision Instruments, UK). Mice were recovered for 3 weeks to allow sufficient time for opsin expression to occur before undergoing Aldara treatment as described above.

Electrophysiology experiments

Drugs and chemicals

CGP55845, DNQX, gabazine, DL-AP5 and picrotoxin were purchased from either Tocris Bioscience (UK) or HelloBio (UK), and all other chemicals were purchased from Sigma-Aldrich (UK) unless otherwise stated.

Brain slice preparation

Mice were deeply anesthetised with 5% isoflurane and the brain was rapidly dissected out in room temperature NMDG cutting solution, containing (in mM): 135 NMDG, 20 choline bicarbonate, 10 glucose, 1.5 $MgCl_2$, 1.2 KH_2PO_4, 1 KCl, 0.5 $CaCl_2$, saturated with 95% O_2 and 5% CO_2 (pH 7.3-7.4). Brains were hemisected and coronal slices (400 um) were cut using a VT-1200S vibratome (Leica Microsystems, Germany) and the slices were transferred into a chamber containing recording aCSF, composed of (in mM): 130 NaCl, 24 $NaHCO_3$, 3.5 KCl, 1.25 NaH_2PO_4, 2.5 $CaCl_2$, 1.5 $MgCl_2$, and 10 glucose, saturated with 95% O_2 and 5% CO_2 (pH 7.4). Slices were placed in a water bath at 37 °C for 30 minutes and slowly cooled to room temperature for further 30 minutes, at which they were maintained until recording.

Patch-clamp recording

For *ex vivo* patch clamp recordings, slices were attached onto 0.1% poly-L-lysine (Sigma Aldrich, P8920) coated glass slides and placed into the upright microscope and visualized using infrared oblique contrast microscopy (Scientifica SliceScope, Scientifica, UK). A CoolLED pE-4000 system (CoolLED, UK) was used to confirm presence of thalamic axons in slices, and to provide optogenetic stimulation. The slices were submerged in recording aCSF, warmed to 32-34 °C, and the rate of perfusion was kept at 5 ml/min. The recording electrodes resistance was typically 4 – 6 MΩ and were pulled from borosilicate glass (World Precision Instruments, UK) using a Sutter P-1000 horizontal puller (Sutter Instruments, CA, USA). The intracellular solution used had the following composition (in mM): 135 Cs-methanesulphonate, 8 NaCl, 10 HEPES, 0.5 EGTA, 4 MgATP, 0.3 Na-GTP, 5 QX314, plus 2 mg/ml biocytin (VWR International, UK), at pH 7.25 adjusted with CsOH to 285 mOsm. Whole-cell recordings in voltage clamp mode were made from ventral striatum, targeting medium spiny neurons (MSNs) based on morphology. Gabazine (10 μM) and CGP55845 (1 μM) were present in the bath throughout recordings to block $GABA_A$ and $GABA_B$- receptor-mediated currents, respectively.

Upon formation of a whole-cell patch, spontaneous activity was recorded for 1 to 2 minutes to sample spontaneous EPSC activity, at a holding potential of -70 mV. A single light pulse was of 470 nm was then applied once every 10 seconds to optogenetically-excite midline thalamic inputs onto ventral MSNs. After a suitable baseline had been established (typically >20 sweeps), 10 μM of AMPA receptor antagonist DNQX was added to the bath to inhibit AMPA-mediated synaptic currents. The holding potential was then switched to +50 mV to allow recording of NMDA receptor-mediated synaptic currents. To confirm the presence of the NMDA current, D-AP5 (100 μM) was added at the end of the recording in a subset of recordings. Whole-cell patch-clamp recordings were made using a Multiclamp 700B amplifier (Molecular Devices, CA, USA). Signals were low-pass filtered at 8 kHz and digitized at 20 kHz using a Digidata 1440A and pClamp 10.2 (Molecular Devices, CA, USA). Recordings were not corrected for the liquid junction potential.

Data Analysis

Electrophysiology data were analysed in ClampFit 11 (Molecular Devices, CA, USA). To measure spontaneous EPSCs, traces were first band-pass filtered in using a high-pass 8 pole Bessel band pass filter at 2Hz and a low-pass Gaussian filter at 1000Hz, and sEPSCs were detected using template matching. For evoked EPSC analysis, data were first baselined to zero and an average was taken of at least 20 traces for both AMPA- and NMDA- receptor-mediated components. The AMPA receptor-mediated EPSC was determined as the maximal EPSC peak at -70mV and NMDA receptor-mediated EPSC as the highest peak at +50 mV. For example trace figure preparation, recordings were imported into Igor Pro (Wavemetrics, OR) using Neuromatic (Thinkrandom, UK). Raw sEPSC traces were band-pass filtered in Igor Pro between 0.1 and 1000 Hz to improve clarity. GraphPad Prism (Graphpad, CA) was used for statistical analysis. Data were tested for normality using the D'Agostino and Pearson test and subsequently analysed by parametric or nonparametric tests as appropriate. Unless otherwise stated, all values are presented as mean ± SEM.

Post hoc morphological recoveries

The tissue slices were post-fixed in 4% PFA solution for an hour after recordings and then transferred to PBS (Melford, UK). Slices were washed thrice in 0.1 M PBS solution, followed by three further washes in PBS with 0.5% Triton X (Sigma, UK). Two blocking steps were used: 100mM of Glycine (Sigma, UK) incubation for 20 mins and then 1-hour long incubation with blocking buffer with 10% goat serum (VectorLabs, UK) at room temperature. Primary antibody against GFP (Abcam, UK) at 1:5000 dilution was used overnight at 4°C; then secondary conjugated anti-chicken antibody (ab150173, Abcam UK) and streptavidin (VectorLabs, UK) were used at 1:250 and 1:500 dilutions respectively were used in a carrier solution containing 10% goat serum and PBS for a two-hour incubation at RT. Finally, the slices were washed thrice in PBS and transferred to 30% sucrose (Thermofisher, UK) until cryoprotected. Then slices were re-sectioned at 100-micron thickness using SM2010R freezing microtome (Leica, UK)) at -20°C and mounted onto glass-slides and HardSet mounting medium with DAPI was used (VectorLabs, UK).

Immunohistochemistry

Mice were given a terminal overdose of the anaesthetic sodium pentobarbitone (Euthatal, 10 µl/g of 200 mg/ml solution) and, once deeply anaesthetised, were killed by transcardial perfusion with PBS followed by 4% paraformaldehyde (Sigma-Aldrich, UK). Following perfusion-fixation, whole brains (n=4 / treatment) were dissected into 4% PFA overnight at 4°C, then cryoprotected in 30% sucrose at 4°C. Coronal sections were cut at 40µm on a SM2010R freezing microtome (Leica, UK) and collected into in-house solution of antifreeze (containing 30% ethylene glycol, 25% glycerol and 25% 0.2M PB in ddH_2O) and stored at -20°C until required. Free-floating sections were washed in PBS then treated with 100% EtOH at -20°C for 10 min, or an antigen retrieval method (overnight at 60°C in 10 mM sodium citrate buffer (pH 6.0)). Tissue was thoroughly washed in PBS, then blocked in PBS containing 10% normal goat serum (NGS) + 0.3% Triton X for 1h at 4°C. Primary antibodies were prepared in PBS containing 3% NGS and applied overnight (or 72 hours in the case of IBA-1, GFAP, VGLUT1 and VGLUT2) at 4°C. Primary antibodies included a combination of the following: rat anti-CD4 antibody (Biolegend, UK, cat# 100505, 1:500), guinea pig anti-IBA1 antibody (Synaptic

Systems, Germany, Cat# 234 308, 1:500), rabbit anti-GFAP antibody (Novus Biologicals, UK, Cat# NB300-141, 1:500), rabbit anti-c-fos (Cell Signalling Technologies, UK, cat # 2250S, 1:500), rabbit anti-VGLUT1 (Synaptic systems, Germany, Cat# 135-302, 1:500), guinea-pig anti-VGLUT2 (Synaptic systems, Germany, Cat# 135-418, 1:250). Sections were washed 3x 10mins in PBS, before the appropriate combination of secondary antibodies were applied for 2h at RT. Secondary antibodies were as follows: isotype-specific Alexa Fluor 488- and Alexa Fluor 546-conjugated goat anti-rat IgG antibodies (Thermo Fisher Scientific Cat# A-21434, RRID:AB_2535855; 1/500), Alexa Fluor 488 goat anti-guinea pig (Abcam, UK, Cat# ab150185, 1:500), Alexa Fluor 594 goat anti-rabbit (Invitrogen, USA, Cat# A11012, 1:500). 3 x 10min PBS washes were followed by mounting in VECTASHIELD® HardSet™ mounting medium with DAPI (Vector Labs, UK, Cat# H-1500-10).

Anatomical tracing of the thalamostriatal projections

Mice that had undergone stereotaxic injections of viral vectors to transduce Chronos-GFP (details below) were killed by perfusion-fixation as described above. Coronal sections were sliced at 50 µm. The slices around the injection coordinates as well as positive control areas (such as prefrontal cortices) and experimental striatal slices were selected and underwent the immunofluorescent staining protocol described above. To enhance visualisation of thalamic axons, sections were incubated with primary antibody against GFP (chicken anti-GFP; Abcam, UK, cat # ab64905, 1:50000) followed by incubation with Alex488-conjugated goat anti-chicken secondary antibody (Abcam, UK, cat # ab150173,1:250). Once stained, the slices were mounted using the HardSet mounting medium containing DAPI (VectorLabs, UK), and images were taken on SLM710 confocal microscope (Zeiss).

Image acquisition and analysis

For immune cell infiltration studies, tile scans of entire coronal brain sections were captured using a widefield inverted Leica DMi8 microscope with a 10x objective. FIJI (ImageJ) software[27] was used to analyse the images as follows: the DAPI channel was used to outline each selected brain region with reference to the Allen brain atlas. The number of CD4+ cells within this measured area were

counted per mouse, the mean plotted and compared per treatment for each region. Criteria for cell inclusion included CD4+ signal, a DAPI nucleus and a diameter of 8-12 µm. Illustrative images were captured using a Zeiss LSM 880 Axio Imager 2 laser-scanning confocal microscope (Zeiss Microscopy, UK) processed using Zen Zeiss Microscopy Software.

For c-fos quantification in the thalamus and VGLUT analysis in the ventral striatum and barrel cortex, confocal z-stacks were captured using a Zeiss LSM 880 Axio Imager 2 laser-scanning confocal microscope equipped with an LD C-Apochromat 20x/1.1 W Korr M27 objective at 0.8 µm optical slice and Plan-Apochromat 63x/1.4 Oil DIC M27 objective at 0.4 µm optical slice, respectively. The same exposure levels were used to capture images from all sections. Quantification of the number of fos-positive cells per ROI was performed in FIJI from maximum intensity z-projections. Quantification of VGLUT positive terminal number and size was performed in FIJI from three 50x50 µm ROIs taken from single z-slices of three sections per mouse.

For analysing the fluorescence signal intensities and coverage areas of IBA-1 and GFAP, confocal z-stack images of IBA-1 and GFAP immunofluorescence were acquired using a Zeiss LSM 880 Axio Imager 2 laser-scanning confocal microscope equipped with an LD C-Apochromat 40x/1.1 W Korr M27 objective (Zeiss, 421867-9970-000) and Immersol W 2010 immersion oil (Zeiss, 444969-0000-000). Each image stack consisted of 16 optical sections spaced 2 µm apart (total depth 30 µm) with a resolution of 2048 x 2048 pixels (354.25 µm x 354.25 µm).

To quantify IBA-1 and GFAP signal intensity and coverage area, the images were first processed the images to subtract the background signals using a 35-pixel rolling ball radius applied to each z-stack in Fiji. Maximum intensity z-projections were then generated, and positive signals isolated using pre-trained pixel classifiers for IBA-1 and GFAP within the LabKit Fiji plugin[28]. The resulting binary masks were used to calculate the percentage area covered by positive signal and to redirect measurements to the original image to measure the mean grey value within the positive signal regions.

Whole brain transcriptome analysis

We carried out a secondary analysis of whole-brain RNAseq transcriptomic data reported in detail elsewhere[29]. In brief, differential expression analysis was carried out DESeq2[30] using pairwise models with no additional covariates. The normalised data were explored using the Searchlight analysis platform[31]. The significance threshold for differential genes was adjusted $p < 0.05$ and absolute log2fold > 0.5. All other parameters were left to default.

Flow cytometry

Mice were given a terminal overdose of the anaesthetic sodium pentobarbitone (Euthatal, 10 µl/g of 200 mg/ml solution) and, once deeply anaesthetised, were killed by transcardial perfusion with 20 ml of ice-cold PBS. Whole brains were dissociated using the Adult Brain Dissociation Kit for mouse (Miltenyi Biotech: Cat. No.:130-107-677, UK) in line with manufacturer's instructions. Briefly, whole brains were cut into 8-10 pieces and placed into a C-tube containing the enzyme mix. Samples were dissociated in the gentleMACSTM Octo Dissociator with heaters using program 37C_ABDK_01 (Miltenyi, UK). Subsequently, samples were filtered through a 70 µm strainer using 10 ml of D-PBS and the back of a 5 ml syringe plunger before being spun at 300 g for 10 min, 4ºC. The supernatant was discarded, and cells were re-suspended in 3.1 ml D-PBS and 900 µl Debris Removal Solution. Another 4 ml of D-PBS was overlain gently, and samples were spun at 3,000 g for 10 min, 4ºC, with half (5) acceleration and half (5) brake. The top two phases, containing debris and myelin, were removed and discarded. D-PBS was added, and cells were centrifuged at 1,000 g for 10 min, 4ºC, and supernatant discarded. Erythrocytes were removed by incubating with 1X Red Blood Cell Removal Solution (provided in the kit) diluted in water for 10min at 4ºC before adding cold PB Buffer. Samples were spun again at 300 g for 10 min, 4ºC and the pellet was dissolved in 1 ml of PBS. Trypan blue and hemacytometer were used for cell counting.

Brain cells were stained in 96-well plate, following protocol with FACS (2% FBS and 0.4% of 50 mM EDTA in 1X PBS) buffer wash and centrifuge spin (400g for 5min at 4ºC) in between each step (all

incubations were performed at 4ºC unless stated otherwise). Live/dead staining (eBioscience™ eFluor™ 506 Catalog number: 65-0866-14, USA) was done in PBS for 20 mins. Fc block (Miltenyi, 130-059-901, UK) step was done for 20 mins and conjugated extracellular antibody (see supplementary table 2) staining was done in FACS buffer for 20 mins. For intracellular staining from T cells, single cells, post extracellular staining, were stimulated with cell stimulation cocktail with protein transport inhibitor (eBioscience™ Cell Stimulation Cocktail (plus protein transport inhibitors) (500X) cat. No. 00-4975-03, USA) for 4 hours at 37 C° in CO_2 incubator. Cells were fixed (Fix buffer, BD Biosciences, USA cat no. 554655) and permeabilised with Perm buffer (BD Biosciences, USA cat. No. 554723) and intracellular staining (see supplementary table 2) was done in perm buffer. For cytokine staining from microglia, astrocytes, and monocytes, only Golgi blocker, Brefeldin, was used for 4 hours. All fluorescence minus one (FMO) staining controls received the full panel staining except for one antibody to determine true populations in the sample (see supplementary table 2) FMOs were generated using pooled sample cells. Compensation was performed with antibody stained UltraComp eBeads (Thermo Fischer Scientific, USA, cat No. 01-2222-41). Flow cytometry was performed at the Cellular analysis facility, MVLS shared research facilities (University of Glasgow) on the LSR Fortessa (BD Biosciences, USA). Data is acquired through BD FACSDiVaTM digital software. All analysis was performed using FlowJo software (v.10.10.0.) (BD Biosciences, USA). Graphs were generated using absolute cell number using the cell counts from haemocytometer and gating strategies percentages (see supplementary methods).

T Cell Depletion experiment

Four cohorts of female C57BL/6J mice (n=4, each cohort) were used for T cell depletion experiment. 2 cohorts were injected with 400 µg of rat IgG (LTF-2) and another 2 cohorts with depleting 200 µg CD4 (GK1.5) and 200 µg CD8 (2.43) antibodies, respectively intra peritoneum (*ip*), three days before starting the control and Aldara cream treatment. Another set of these blocking antibodies were administered i.p. couple of hours before the 2nd day of cream treatment. Tissue collection was performed after the final (3rd day) cream application, as described above.

Immunoblotting

Whole brain homogenates were prepared using RIPA buffer with protease and phosphatase inhibitor. Samples were run on 4 - 12% gradient gel and transferred to nitrocellulose membrane. 5% milk in TBS-tween was used for 1hr blocking. Anti IL-1b (mouse, 1:1000) and NLRP3 (rabbit, 1:1000) were used with anti-mouse secondary antibody. A-tubulin was used as loading control.

NLRP3 inhibition

We used brain penetrant NLRP3 inhibitor, NT-0527 (NodThera, UK) at 100 mg/kg in a vehicle composed of 0.5% methyl cellulose (cat. # M7410; Sigma-Aldrich, UK) and 0.2% Tween 80 (cat. #P4780; Sigma-Aldrich, UK). Mice were dosed with drug (20 mg/ml) or vehicle via oral gavage, starting one day prior to Aldara treatment, and continued for all three days of the treatment, an hour before applying the cream. Tissues were harvested after final day (3rd day) of cream application, as described above.

Statistical analysis

Data were checked for normality using Shapiro-Wilk's test and parametric tests were used throughout, unless otherwise specified; outliers were tested for using ROUT test. No animals were excluded from the data analysis. Comparisons were made using either unpaired two-tailed t-test (e.g. For total average speed in EPM maze for control and Aldara-treated animals) or one-way ANOVA with *post hoc* multiple comparisons with Tukey correction. Data are presented as mean ± SEM unless otherwise stated. Unless otherwise stated, the numbers of independent animals are described per experiment above and indicated in the figure legends. Statistical differences were determined using GraphPad Prism software (GraphPad Prism, RRID:SCR_002798).

Results

Behavioural assessment of mice following 3 days Aldara treatment

We carried out behavioural testing to ascertain whether the neuroinflammation induced by topical application of Aldara cream over 3 days induced changes in reward and motivation phenotypes and

anxiety-like behaviour. We used the nest-building assay[23] as a measure of intrinsic motivation in mice. Mice were provided with 3.0 g nestlet each evening and we measured the amount of unused nestlet the following morning. After 3 days of treatment, we observed a significant increase in the amount of unused nestlet in Aldara-treated mice relative to controls (Fig. 1A). Additionally, the quality rating of the nest built by the mice over the 24h period progressively decreased in Aldara-treated mice, reaching significance at day 3 post-treatment (Fig. 1B). In contrast, control mice displayed a trend for a progressive improvement in nest quality. Examples of nests, corresponding to each of the possible grades for nest-building assay, are shown in Supplementary Fig. 1. Overall, this test suggested a reduction in intrinsic motivation in Aldara-treated mice.

To further assay anhedonia-like behaviour, we used the sucrose preference test. We measured the sucrose-to-water ratio (weight change in sucrose solution divided by the weight change in water solution in the previous 12 hours) twice daily, to account for the nocturnal cycle of mice: their baseline preference for sucrose was absent during the daytime (typical ratio of 1 for both groups) but was on average ~4 during the night in both groups. Aldara treatment significantly reduced the preference for sucrose at night, relative to control-treated mice (Fig. 1C). Together, the nest-building assay and sucrose preference test indicate an emerging anhedonia-like phenotype after 3 days treatment with Aldara.

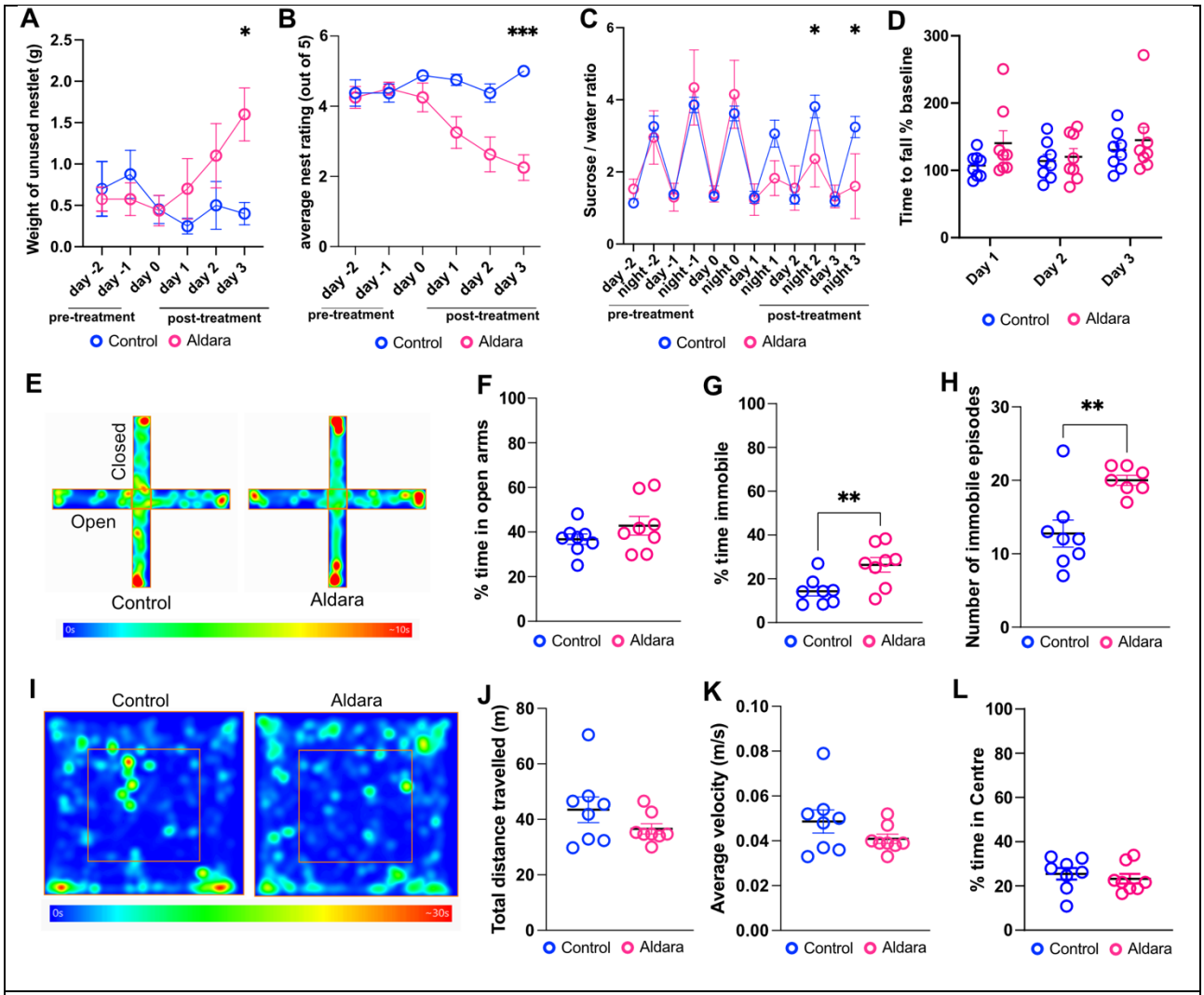

Figure 1: Behavioural assessment of 3-day Aldara-treated mice. In all panels control mice are shown in blue and Aldara-treated mice in pink. **A**, Nest-building assay across treatment time: significant interaction between Aldara treatment with time on amount of unused nestlet ($p = 0.0079$ in 2-way repeated measures ANOVA), with a significantly more unused nestlet in Aldara-treated mice by day 3 (control *vs* Aldara-treated 1.1 ± 0.2 g *vs* 0.38 ± 0.1 g, $p = 0.0403$ in *post hoc* Šídák's multiple comparisons). **B**, Aldara treatment caused increasingly lower nest-building ratings across time which reached significance on day 3 (Effect of treatment: $p = 0.0007$; effect of time: 0.0067; interaction: $p < 0.0001$; Two-way ANOVA with Šídák's *post hoc* tests; 5 is highest and 1 is lowest). **C**, Sucrose preference at day and night during treatment. Significant interaction between treatment and time ($p < 0.0001$; Two-way ANOVA) with Aldara-treated mice showing significantly less preference for sucrose during the night after 2 and 3 days of treatment (Šídák's *post hoc* tests). **D**, Rotarod performance (% time to fall from the rod compared to baseline) was evaluated every day prior to cream treatment, control *vs* Aldara-treated 117.1 ± 11.73 vs 135.1 ± 13.2 % show no significant change as found with a Two-way ANOVA. **E**, Representative heatmaps from elevated plus maze (EPM) recordings performed 24h following final treatment. **F**, Percentage time spent

in open arms of the EPM was not changed, p = 0.2276, unpaired two-tailed t-test. **G**, Percentage time spent immobile (immobility defined as not moving for longer than 2 seconds) in 5-minute trial, control *vs* Aldara-treated p = 0.0093, unpaired two-tailed t-test. **H**, Total number of immobile episodes during EPM testing, p = 0.0039, unpaired two-tailed t-test. **I**, Representative examples of heatmaps of open field (OF) exploration for control and Aldara-treated mice. **J**, Total distance travelled during OF testing, control *vs* Aldara-treated 41.87 ± 13.3 *vs* 38.57 ± 6.6 m, p = 0.7984, Mann-Whitney test. **K**, Average velocity of mice during OF testing, control *vs* Aldara-treated 0.049 ± 0.01 *vs* 0.041 ± 0.006 m/s, p = 0.1869, Mann-Whitney test. **L**, Percentage time spent in the centre of OF maze, control *vs* Aldara-treated 25.49 ± 7.4 *vs* 23.22 ± 6.3, p = 0.5198, unpaired t test. Scatter plots display data points (each point is one animal) and mean ± SEM; n=8 mice per group in all tests; *, p < 0.05; **p < 0.01; *** p < 0.005.

We used the rotarod test to assess motor capability in evoked movement in Aldara-treated mice. There was no significant difference in rotarod performance (time to fall relative to baseline) between treatment groups (Fig. 1D), demonstrating there were no motor impairment due to Aldara treatment. We sought to determine whether Aldara treatment also produced anxiety-like behaviours. We used the elevated plus maze (EPM) as a primary measure of anxiety. Both groups of mice spent less time in open arms than the closed arms (example heat-maps in Fig. 1E), with Aldara-treated animals showing no difference in percentage of time in open arms relative to control-treated mice (Fig. 1F). Interestingly, however, Aldara-treated mice spent a significantly longer period immobile (Fig. 1G) relative to control mice. Additionally, these mice exhibited a significantly greater number of immobile periods (Fig. 1H) on the elevated plus maze than control mice, demonstrating a start-stop like activity within the test. Further EPM data are presented in supplementary Fig. 1. Combining the EPM and rotarod data, it appears that while Aldara treatment did not induce an anxiety-like phenotype and mice behaved normally when forced to move, there appeared to be a reduction in self-driven exploratory movement in the EPM. This observation further reinforces the conclusion that Aldara treatment appears to lead to reduced motivation in mice.

On open field test, carried out in the afternoon on the same day as EPM, Aldara-treated mice displayed no evidence of changes in locomotor activity relative to controls, measured as total distance travelled in the maze (Fig. 1J) or as total velocity in the maze (Fig 1K). Both groups exhibited

a preference for the perimeter of the open field maze over the centre (Supplementary Fig. 1), but Aldara-treated mice did not display any difference in percentage of time spent in the centre (a proxy measure of anxiety) relative to controls (Fig 1L). Unlike in EPM, Aldara-treated mice did not display significant reductions in self-driven movement in the open field test. This may be due to EPM being carried out first in the morning (immediately after mice had finished their active period) but mice subsequently having had ~5 hours of sleep by the start of open field testing.

Neuroinflammation changes neuronal activation in a region-specific manner

To understand how Aldara-driven neuroinflammation alters neural circuit function, we first assayed neural activity using immunohistochemistry for the immediate early gene product c-Fos, an established marker of neuronal activity. We measured c-Fos activity 4 hours after treatment with Aldara, having previously shown via mass spectrometry that Aldara enters the brain within this time period[20]. Connections between midline thalamus, ventral striatum / nucleus accumbens and prefrontal areas are an important part of the reward circuitry that is implicated in anhedonia and depression[32]. We found evidence of a significant increase in c-Fos activity within the midline thalamus of Aldara-treated mice relative to controls (Fig 2A – B). We next used anatomical methods to quantify glutamate transporters in ventral striatum after 3 days of Aldara treatment, when behavioural effects were most pronounced. Ventral striatum receives input from both prefrontal cortex and midline thalamus, so we used immunofluorescence to visualise glutamate transporters VGlut1 and VGlut2, which are preferentially expressed on cortical and thalamic axons, respectively[33], to parse these two striatal inputs (Fig. 2C). We chose vS1 as a control region to the strong thalamic innervation of layer 4 in the barrel cortex (Fig. 2E). We found a significant increase in the number (Fig. 2D) and size (Fig. 2E) of VGlut2 axon terminals in ventral striatum but not vS1, and observed no significant changes in VGlut1-containing axon terminals. These data suggest that there was a change in the thalamic, but not cortical, inputs to ventral striatum and the lack of change in vS1 suggests that this was specific to the reward pathway. We next sought to further categorise these changes using electrophysiology.

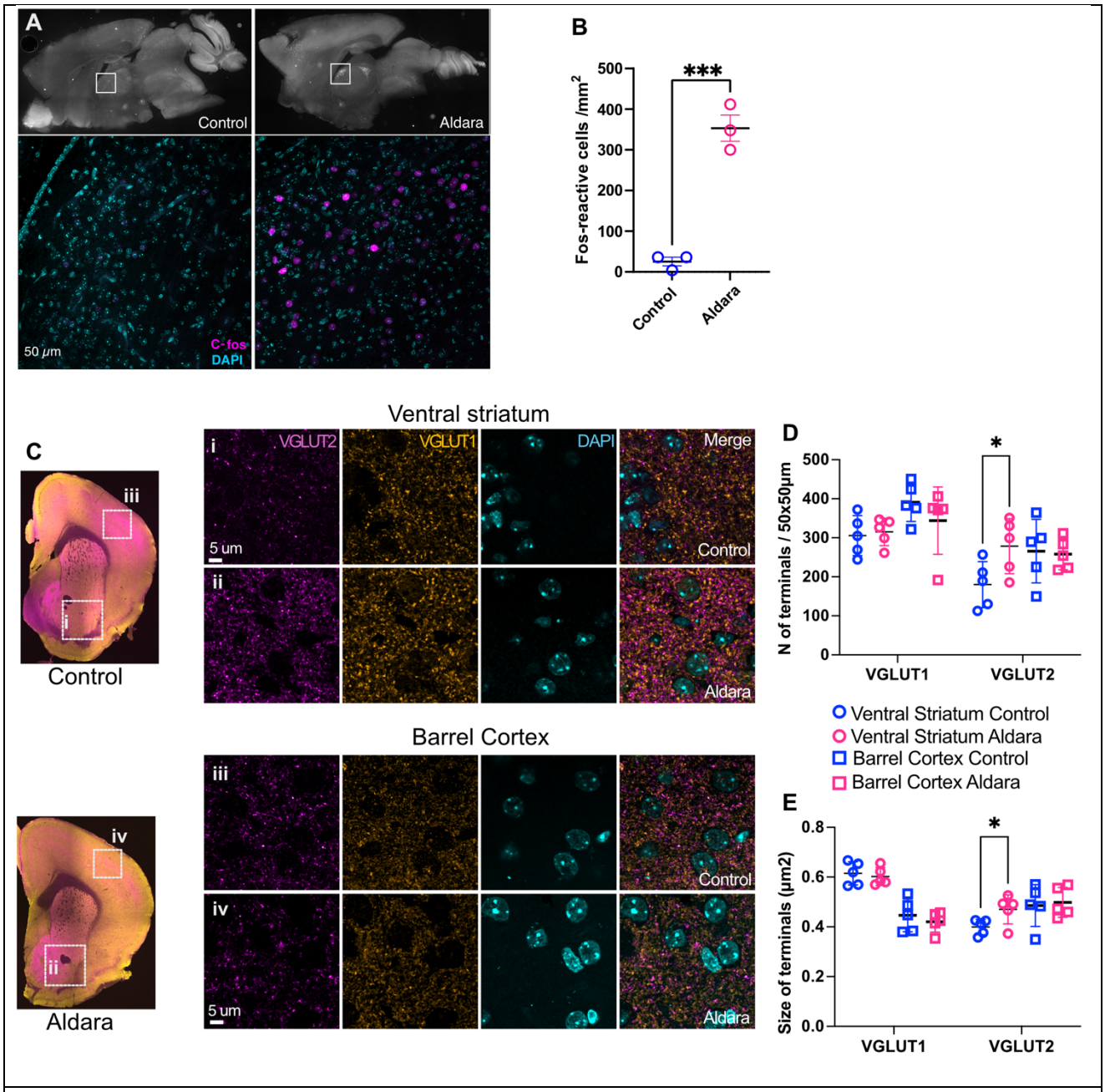

Figure 2: Region-specific changes in c-Fos activation and VGlut1 and VGlut2 expression in Aldara-treated mice. A, Representative images from control and Aldara-treated brain showing fos-positive nuclei (magenta). Scale bar 50 micron. **B,** A significant increase in fos-reactive nuclei in the thalamus 4 hours post treatment, control *vs* Aldara-treated 25.33 ± 18.5 *vs* 353.3 ± 56.2, p = 0.0007, unpaired t-test. **C,** Representative images of VGlut1 and VGlut2 expressing terminals in control (**Ci&Ciii**) and Aldara (**Cii&Civ**) in ventral striatum (**Ci&Cii**) and barrel cortex (**Ciii&Civ**). Scale bar 5 microns. **D,** Number of VGlut2 but not VGlut1 positive terminals in ventral striatum, but not barrel cortex increases in Aldara-treated mice. VGlut1 305.6 ± 51.2 *vs* 315.1 ± 35.2 in ventral striatum; 391.2 ± 39.4 *vs* 343.9 ± 86.2 in barrel cortex; VGlut2 180.0 ± 59.1 *vs* 278.5 ± 70.3 in ventral striatum; p = 0.0251 in *post hoc* Šídák's multiple comparisons test after two-way ANOVA; VGlut2 365.7 ± 81.5 *vs* 258.1 ± 40.0 in barrel cortex. **E,** Size of VGlut2 but not VGlut1 positive terminals in ventral striatum

but not barrel cortex increases in Aldara-treated mice. VGlut1 0.615 ± 0.047 *vs* 0.602 ± 0.036 in ventral striatum; 0.446 ± 0.067 *vs* 0.420 ± 0.041 in barrel cortex; VGlut2 0.400 ± 0.031 *vs* 0.470 ± 0.058 in ventral striatum; p = 0.0451 in *post hoc* Šídák's multiple comparisons test after two-way ANOVA; VGlut2 0.486 ± 0.084 *vs* 0.498 ± 0.060 in barrel cortex.

Neuroinflammation drives functional changes in thalamostriatal circuitry

The mouse immunohistochemistry experiments suggested a specific change in thalamostriatal connectivity. To explore this in humans, we analysed functional fMRI imaging in people with PsD (Fig 3A) to assess the relationship between this circuitry and depressive symptoms. We observed a significant positive correlation in functional connectivity between left thalamus and right nucleus accumbens and PROMIS depression score (Fig. 3Ai). Additionally, we saw non-significant but trending-positive correlation between thalamic ALFF (a proxy measure of spontaneous activity[25]) and depression score (Fig. 3Aii). These data align with a recent human neuroimaging study that found higher connectivity between paraventricular thalamic nucleus and ventral striatum in individuals with anhedonia[34] .

To determine whether mice displayed similar changes in thalamostriatal connectivity, we carried out stereotaxic surgeries to deliver AAV vectors to transduce expression of the excitatory opsin Chronos-GFP[35] to neurons in midline thalamus, with an injection site targeting the border of PVT and CM (Fig 3). This led to widespread expression of Chronos-GFP in thalamic axons spread throughout ventral striatal regions including nucleus accumbens (Fig. 3C – F). We made patch-clamp recordings in voltage-clamp mode from medium spiny neurons (MSNs) in ventral striatum, confirmed using *post hoc* morphological recovery (Fig. 3G & H). We found a significant reduction in the AMPA receptor-mediated component of the midline thalamic EPSC onto ventral MSNs in Aldara-treated mice relative to controls (Fig. 3I & K). However, we found no statistically significant reduction in the NMDA receptor-mediated component of the EPSC (Fig. 3I & L). While the statistical test did not reach the threshold for significance, the data appeared to be trending towards a reduction in Aldara treatment, with the lack of significance likely due to a lower sample size available for this part of the study. Indeed, we saw no significant change in the ratio of AMPA/NMDA currents due to Aldara treatment,

supporting the conclusion that both glutamatergic currents were likely reduced after Aldara treatment (Fig. 3M).

To test whether the neuroinflammation-driven change in thalamic EPSC may be due to altered presynaptic release, we examined spontaneous EPSCs of ventral MSNs (Fig 3J). We found no significant effect of Aldara treatment on either the amplitude (Fig. 3N) or frequency (Fig. 3O) of spontaneous EPSCs. Finally, we found that treatment with Aldara did not significantly alter the input resistance of MSNs (input resistance, control (n=17) *vs* treated (n=26): 65.2 ± 6.3 MΩ *vs* 62.5 ± 6.2 MΩ; $p = 0.4057$, Mann-Whitney test), suggesting no change in intrinsic excitability of MSNs.

We carried out secondary analysis of our whole brain RNAseq transcriptomic dataset[29] to gain further insights into the potential neurobiological mechanisms underlying the impairment in the thalamostriatal EPSC. We previously observed global downregulation in neurotransmission-associated genes and regional changes in specific transmitter gene expression[29]. Here, we examined the expression of selected individual genes, covering a range of neurotransmitter receptor subunits, synthesis and metabolism, and neurotransmitter transporters (Fig. 3B). There was a general trend of downregulation in the majority of these gene sets, with significant downregulation of genes encoding GluN1 and GluN2C subunits of the NMDA receptor. There were no significant changes in AMPA, kainate or dopamine receptor subunit expression but, interestingly, both *Homer1* and *Homer2* were significantly downregulated on a brain-wide basis, implying disruption to maintenance of glutamatergic synapses[36]. Genes involved in glutamate synthesis and metabolism, *Glul* and *Gls* were significantly downregulated. Of the amino acid transporters, only the astrocyte-specific EAAT2 (encoded by *Slc1a2*) was significantly downregulated, implying an impairment in astrocytic glutamate reuptake. We also saw significant downregulation of tyrosine hydroxylase but no changes in any monoamine transporter genes, implying potential early disruption of dopaminergic reward circuitry or impairments in other monoamine signalling.

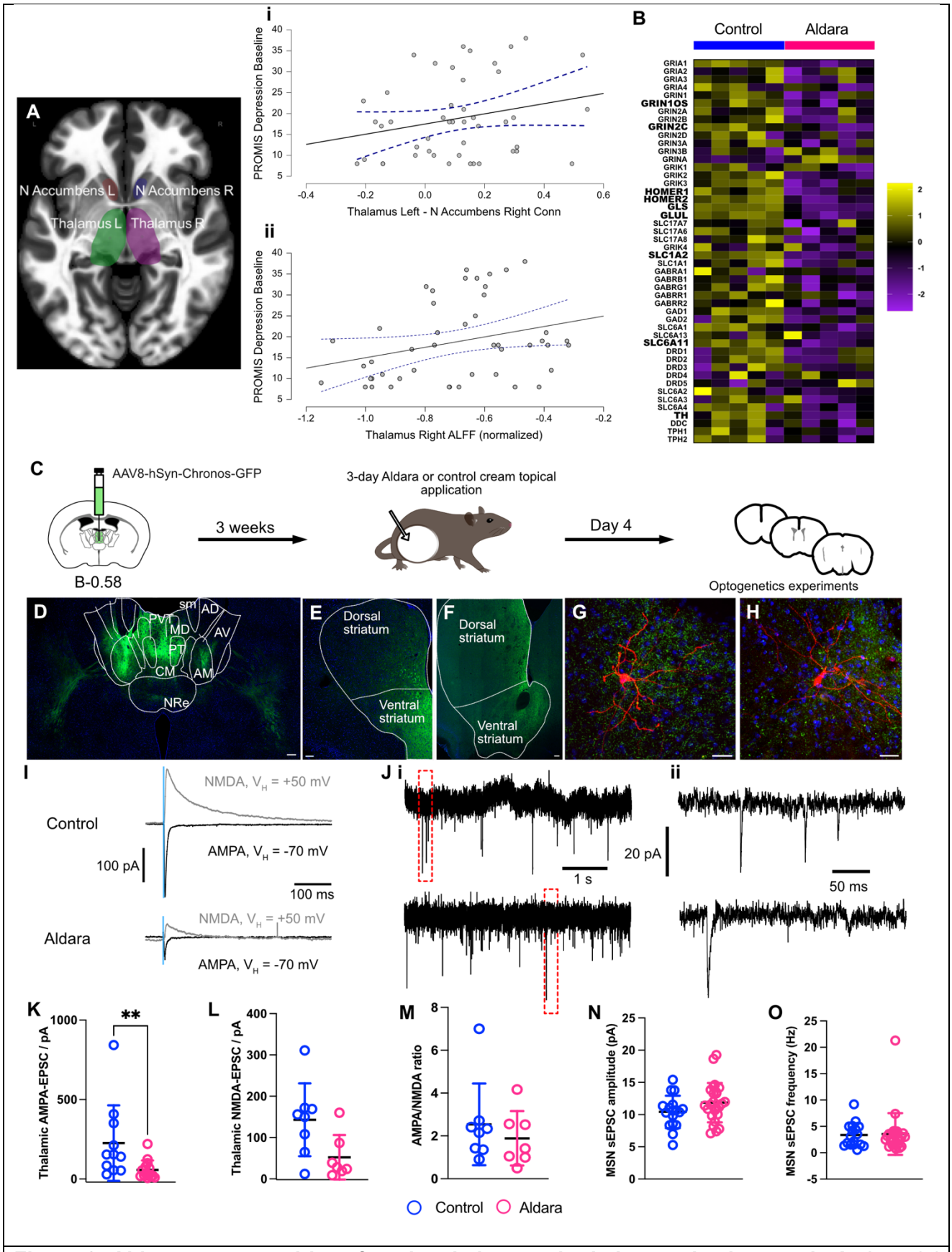

Figure 3: Aldara treatment drives functional changes in thalamostriatal network. A, An axial slice (x = 10, y = -18, z = -6) of an MNI template with the four regions-of-interest (ROIs): the bilateral nucleus accumbens and thalamus, based on the Harvard-Oxford Atlas. **i**, Thalamostriatal functional

connectivity positively correlates with PROMIS Depression scores (β = 0.355, p = 0.02) of patients with PsA (n = 46), after controlling for age and gender (24 female, mean ± SD age = 49 ± 11.2); **ii**, spontaneous functional activity of the right thalamus shows a trend towards significance of positively correlating with PROMIS Depression scores (β = 0.244, p = 0.09) using normalized amplitude of low-frequency fluctuations (ALFF) values. **B**, Changes in expression for selected neurotransmission-related genes in bulk RNAseq samples after 3 days of Aldara treatment. Significant differences shown in bold. Scale bar indicates direction of change. **C**, Schematic of experimental design for optogenetic and *ex vivo* patch clamp electrophysiology experiments investigating effect of Aldara treatment on midline thalamus projections to ventral MSNs. **D,** Representative image of midline thalamus showing expression of AAV8-hSyn-Chronos-GFP vector 3 weeks after injection. **E & F**, Expression of thalamic fibres in rostral and caudal portions of striatum, respectively. **G**, *Post hoc* recovery of biocytin-filled MSN in ventral striatum (red) with thalamic axons expressing Chronos-GFP (green); DAPI stain in blue. **H**, Representative traces of voltage-clamp electrophysiological recordings showing AMPA and NMDA receptor-mediated components of the optogenetics-evoked midline thalamic EPSC onto MSNs in the ventral striatum for control (top) and Aldara-treated (bottom) mice. **I**, Spontaneous EPSCs on ventral MSNs for control (top) and Aldara-treated mice (bottom) recorded in voltage clamp mode (V_H = -70 mV). Red hatched area in **i** shown in **ii** on an expanded time base. **J**, Aldara treatment caused a significant reduction in the AMPA-receptor mediated thalamic EPSC, control (**i**) *vs* Aldara-treated (**ii**): 225.9 ± 71.7 pA *vs* 57.07 ± 15.9 pA, p = 0.0013, as measured with Mixed effects analysis; but **K,** had no statistically significant effect on the NMDA-receptor mediated component, control *vs* Aldara-treated: 142.9 ± 31.2 pA *vs* 52.29 ± 20.3 pA, p = 0.3486, as measured with mixed effects analysis. **L,** Aldara treatment had no significant effect on the AMPA/NMDA ratio of the thalamic input into ventral MSNs, control *vs* Aldara-treated: 2.54 ± 0.67 *vs* 1.89 ± 0.5, p = 0.6126, as measured with Mann- Whitney test. **M & N**, Aldara treatment had no effect on the amplitude or frequency, respectively, of sEPSCs in ventral MSNs: control *vs* Aldara-treated 10.4 ± 0.6 pA *vs* 11.9 ± 0.6 pA; p = 0.1014, Mann-Whitney test (amplitude). Control *vs* Aldara-treated 3.4 ± 0.5 Hz ± 3.5 ± 0.8 Hz; p = 0.6481, Mann-Whitney test (frequency). *Abbreviations: AD, anterodorsal thalamus; AM, anteromedial thalamus; AV, anteroventral thalamus; CM, centromedial thalamus; MD, mediodorsal thalamus; NRe, nucleus reuniens; PVT, paraventricular thalamic nucleus.* All data taken from at least 4 mice per group (6 mice for eEPSC data) across 3 different litters, with only 1 neuron taken per brain slice.

Neuroinflammation drives functional changes in glial cells

To ascertain whether Aldara treatment drives functional changes in astrocytes and microglia, we performed flow cytometry and immunostaining. IBA-1 immunohistochemistry experiments revealed changes in microglial morphology (less ramified, more amoeboid) indicative of reactivity (Fig. 4A). However, there were no significant quantitative changes in IBA-1 average fluorescence intensity (Fig. 4B) or total area covered by IBA-1 (Fig. 4C), with hippocampus being the only region showing a significant increase relative to control mice. Flow cytometry gating with $CD45^{int}$ and $CD11b^{hi}$ for microglia showed increases in the total number of microglia in Aldara treated compared to controls (Fig 4D). Similarly, activated microglia markers, MSR1, F4/80 and MHCII (Fig. 4E) all confirmed the increased number of reactive microglia in Aldara-treated mice. Transcriptomic analysis of our previously reported data[29] confirmed that several genes associated with microglial activation were upregulated in Aldara-treated mice (Supplementary Fig. 3A).

Conversely, immunohistochemistry staining with GFAP did not show major changes in astrocyte immunoreactivity or morphology in response to Aldara treatment (Fig. 4F), nor were there changes in average GFAP intensity (Fig. 4G) or area covered (Fig. 4H). GFAP, S100β and ACSA2 (Fig. 4I) were used as markers to identify potential astrocytic activation in flow cytometry, but we found little evidence of differences in the individual expression profile of these three markers in the treated brains compared to control. However, there was a significant increase in the number of triple-positive astrocytes for GFAP, S100β and ACSA2 (Fig. 4J) in the Aldara treated mouse brains, which could provide putative evidence of reactivity. Transcriptomic analysis also found upregulation of genes associated with astrocytic activation in Aldara-treated mice (Supplementary Fig.3B). In summary, we found strong evidence of microglial reactivity and weak evidence suggesting astrocytic reactivity in response to Aldara treatment.

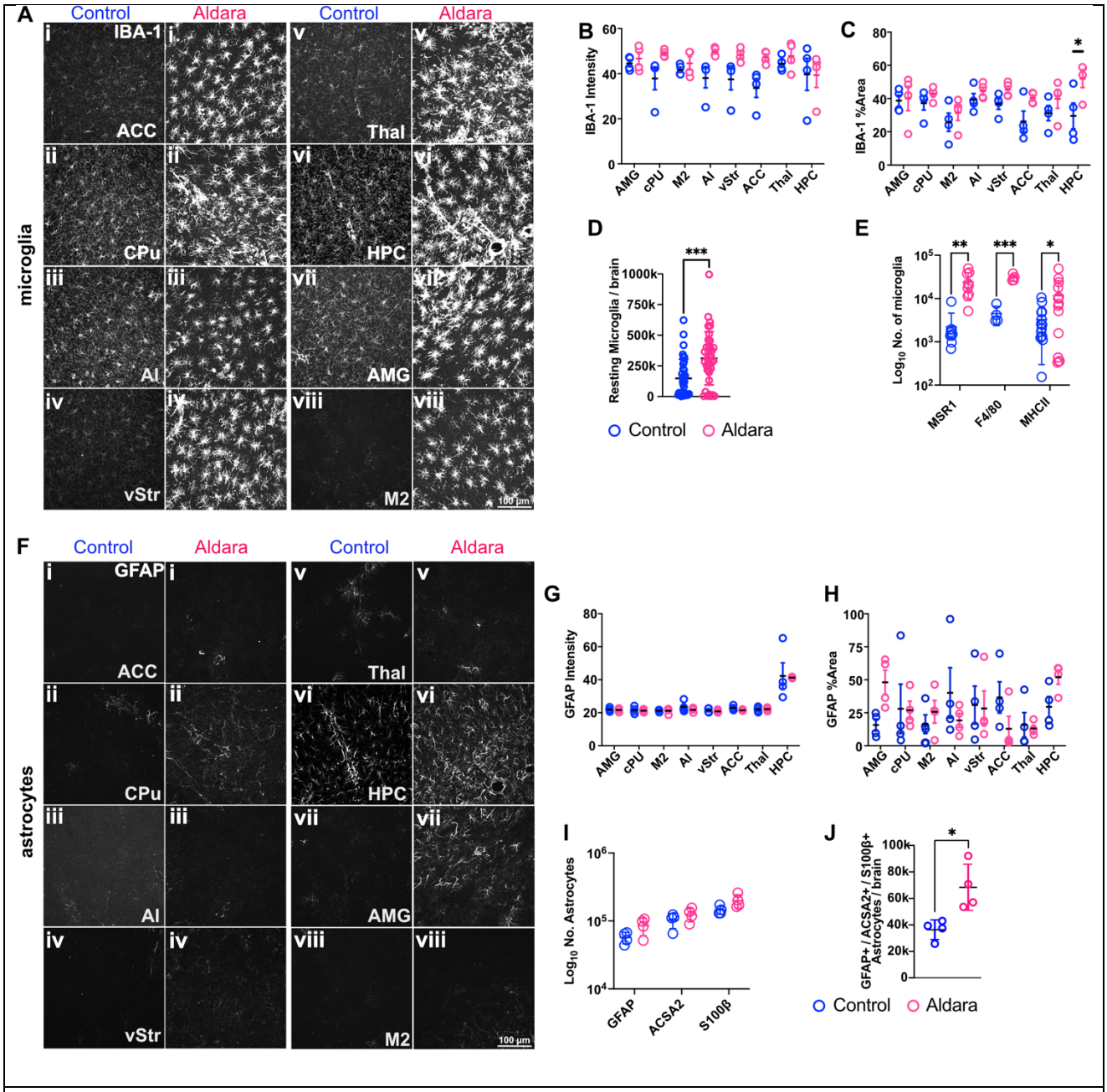

Figure 4: Alterations in microglia and astrocytes following Aldara treatment. In all panels control mice are shown in blue and Aldara-treated mice in pink. **A**, images taken from immunohistochemistry stain for IBA1 in control- and Aldara-treated brains for: **i**, anterior cingulate cortex (ACC); **ii**, caudate putamen/dorsal striatum (CPu); **iii**, agranular insular cortex (AI); **iv**, nucleus accumbens/ventral striatum (vStr); **v**, midline thalamus (thal); **vi**, dorsal hippocampus (HPC); **vii**, amygdala (AMG); **viii**, motor cortex (M2). **B**, average density of IBA1 stain (on an 8-bit scale, so 0 to 255) for control- and Aldara-treated brains. **C**, total % area of section labelled for IBA1, [insert stats]. **D&E**, flow cytometry counts for total number of cells in brain homogenate from control- and Aldara-treated mice, selecting for the following microglia markers: total resting microglia (CD45int and CD11bhi; (Control *vs* Aldara 165242 ± 158635 *vs* 313437 ±229741 $p < 0.0001$, two-tailed t-test. **D**), MSR1, F4/80 and MCHII 2221 ± 2391 *vs* 24098 ± 15110 for MSR1, $p = 0.0024$, 4499 ± 2130 *vs* 30549 ± 5389 for F4/80, $p = 0.0009$, 3283 ± 2985 *vs* 11665 ± 14100, $p = 0.0470$, in *post hoc* Šídák's

multiple comparisons test after two-way ANOVA. (**E**). **F,** images taken from immunohistochemistry stain for GFAP in control- and Aldara-treated brains for same regions as **A**. **G**, average density of GFAP stain (on an 8-bit scale, so 0 to 255) for control- and Aldara-treated brains. H, total % area of section labelled for GFAP for same samples. **I**, flow cytometry counts for total number of cells in brain homogenate from control- and Aldara-treated mice, positive for GFAP, ACSA2 and S100β astrocytic markers. 57040 ± 10912 *vs* 85302 ± 24515 (GFAP), 103243 ± 25997 *vs* 124847 ± 28099 (ACSA2), 144611 ± 19643 *vs* 198835 ± 43995, no significant changes as found in *post hoc* Šídák's multiple comparisons test after two-way ANOVA. **J**, GFAP / ACSA2 / S100β triple positives. *, $p < 0.05$; ***, $p < 0.005$.

Immune cell infiltration into the brain following Aldara treatment

We have previously shown that 3 days of treatment with Aldara results in an ingress of immune cells into the brain[21]. Flow cytometry and immunohistochemistry experiments determined which immune cell type(s) were entering the brain. These data are summarised in Fig. 5, and our gating strategies for all following flow cytometry experiments are provided in supplementary materials. Flow cytometry of brain single-cell homogenates showed expression of 4 key populations based on two classical makers CD45 and CD11b (Fig. 5A). The four cell populations were: non-immune ($CD45^{-}CD11b^{-}$); lymphoid ($CD45^{+}CD11b^{-}$); myeloid ($CD45^{hi}CD11b^{+}$); and microglia ($CD45^{int}CD11b$)[37].

Aldara treatment caused a substantial increase in both lymphoid, myeloid and microglial cells in brain homogenates (Fig. 5A) with an overall increase in the total number of cells (Fig. 5B) relative to controls. This increase was attributable to CD45+ (Fig. 5C). Of the peripheral immune cells infiltrating the brain, this population was primarily comprised of monocytes, B cells, NK, and NKT cells (Fig. 5D; note that data are plotted on a logarithmic scale). Flow cytometry also showed an increase in $CD3^{+}$ T cells in the brain following Aldara treatment (Fig. 5E) and, of these, we saw significantly increased level of $CD4^{+}$ and $CD8^{+}$ T cells (Fig. 5E – F). Regionality of infiltrating T cells was assessed using immunohistochemistry. We found a uniform increase in $CD4^{+}$ cells in all brain regions tested (Fig. 5G – 5H), although the density of $CD4^{+}$ T cells did not reach significance on *post hoc* multiple comparisons tests for hippocampus and ventral striatum (Fig. 5H). Thus, both flow cytometry and immunohistochemistry confirm that Aldara treatment is associated with substantial peripheral immune cell ingress into the brain, with an apparently uniform brain parenchymal penetration.

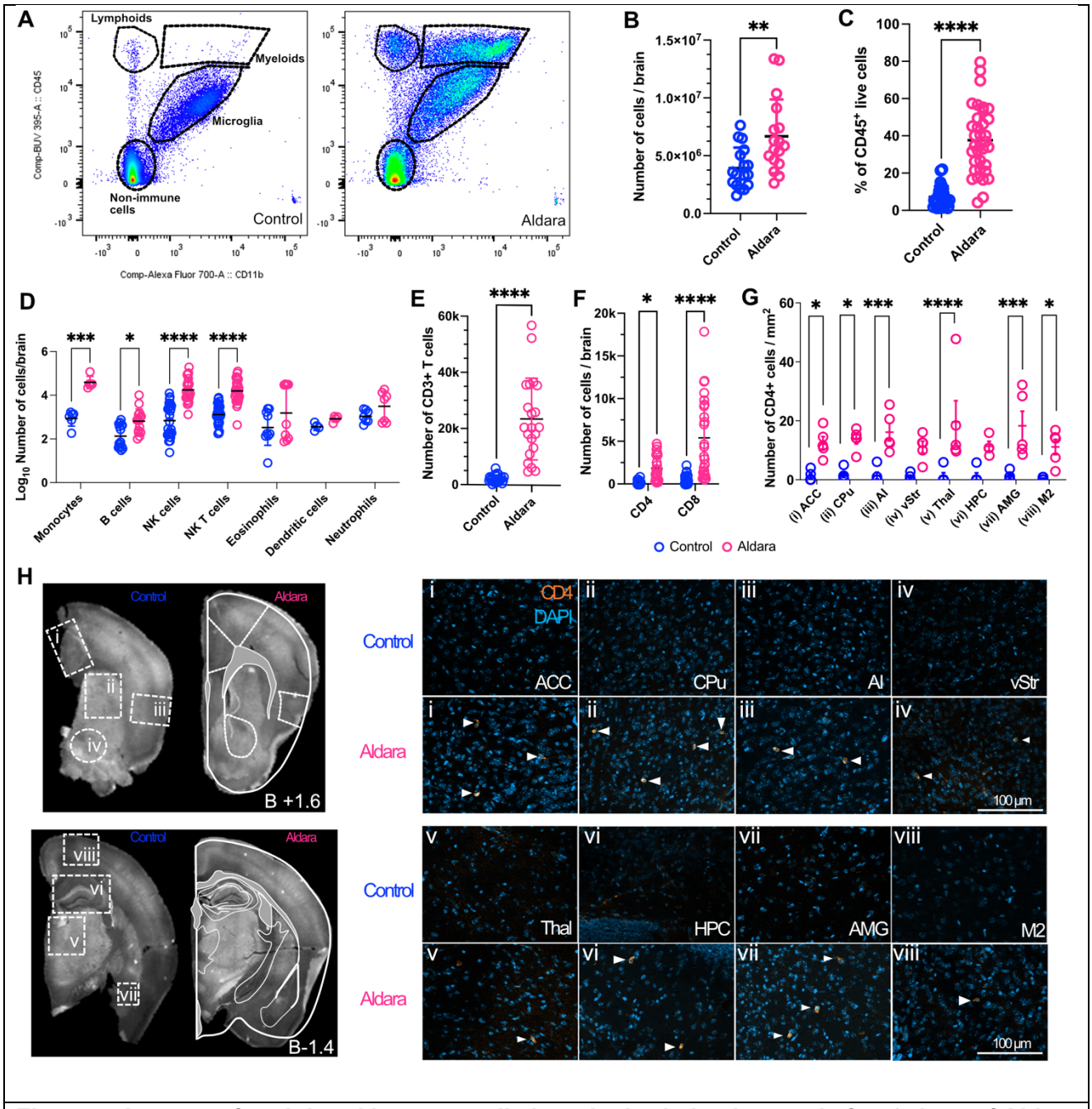

Figure 5: Ingress of peripheral immune cells into the brain is observed after 3 days of Aldara treatment. In all panels, control mice are shown in blue and Aldara-treated mice in pink. **A,** Representative basic flow cytometry panels from a single control (left) and Aldara-treated (right) brain. The 4 broad cell types are indicated within dashed lines. **B,** total number of cells ($10^{\wedge 6}$) found in the brain homogenates from control and Aldara-treated mice, n=17 4± 2 *vs* 7 + 3 p = 0.0039, unpaired t-test. **C,** relative proportion of live CD45+ cells in control- and Aldara-treated brain homogenates control *vs* treated 38 ± 3% *vs* 7 ± 1%, n=36 mice per group; p < 0.0001, unpaired t-test. **D,** numbers of different immune cell types, as measured with flow cytometry, in control- and Aldara-treated brain homogenates (data plotted on log scale) Monocytes n=6 1061 ± 533 *vs* 47317 ± 40268 p < 0.0001; B cells n= 15 248 ± 245 *vs* 1510 ± 2593 p = 0.0170; NK cells n= 27 2172 ± 2995 *vs* 34584 ± 44310 p < 0.0001; NK T cells n= 27 2068 ± 2030 *vs* 28573 ± 31534 p < 0.0001;

Eosinophils n= 9 9257 ± 1021 *vs* 13923 ± 16315 p = 0.1606; Dendritic cells n= 4 349 ± 148 *vs* 871 ± 255 p = 0.9825; Neutrophils n= 7 1295 ± 791 *vs* 7016 ± 7079 p = 0.7446 as shown by Sidak's multiple comparison test. **E,** absolute numbers of CD3-expressing T-cells in control and Aldara-treated mice n=21 control *vs* treated 2150± 1320 *vs* 23579 ± 14547 p < 0.0001 unpaired t-test **F,** Aldara treatment led to a significant increase in the numbers ($10^{\wedge 3}$) of CD4 and CD8 expressing T – cells CD4 T cells, n=24 control vs treated 188 ± 192 *vs* 1850 ± 1461 p = 0.0245 and CD8 T cells control vs treated 478 ± 563 *vs* 5402 ± 4781 p < 0.0001 as shown by two-way ANOVA. **G,** Summary immunohistochemistry data for density of CD4+ T cells in multiple brain regions from control versus Aldara-treated brain sections: **i**, anterior cingulate cortex (ACC) n=5 1.2 ± 1.8 *vs* 12.5 ± 4.7 p<0.05; **ii**, caudate putamen/dorsal striatum (CPu) n=5 1.6 ± 1.97 *vs* 13.7 ± 3.6 p<0.05; **iii**, agranular insular cortex (AI) n=5 1.4 ± 2.7 *vs* 16.1 ± 6.7 p<0.001; **iv**, nucleus accumbens/ventral striatum (vStr) n=5 0.8 ± 1.2 *vs* 11.1 ± 4.4 p=0.0608; **v**, midline thalamus (thal) n=5 1.2 ± 2.6 *vs* 19.6 ± 16.1 p<0.001; **vi**, dorsal hippocampus (HPC) n=5 1.2 ± 2.6 *vs* 11.4 ± 3.3 p=0.0965; **vii**, amygdala (AMG) n=5 1.1 ± 1.5 *vs* 18.3 ± 11.1 p<0.001; **viii**, motor cortex (M2) n=5 0.4 ± 0.5 *vs* 11.1 ± 5.7 p<0.05. **H,** Representative example of coronal slices taken from anterior (Bregma +1.6, left) and posterior (Bregma -1.4, right) brains. Brain regions for CD4+ quantification are highlighted. Representative images of each region from control and Aldara-treated brain sections are shown (CD4 orange, DAPI blue), positive cells are indicated by white arrowheads. Scale = 100 µm. Each point represents an individual animal (4 animals per experiment and cumulative at least 4 – 5 experiments per flow result), mean ± S.E.M. Unpaired t-tests (with or without Welsch's correction as appropriate) were carried out on data from B, C, E, F; two-way ANOVAs were carried out on data on D and G. *, p < 0.05; **, p < 0.01; ***, p < 0.005; ****, p < 0.0001.

Pro-inflammatory cellular response following Aldara treatment

Using flow cytometry, we found significant increases in subsets of infiltrating $CD4^+$ and $CD8^+$ T cells in brain of treated mice relative to controls, with increases in Th1/Tc1 cells secreting TNFα, but with no Th2 cells secreting the anti-inflammatory IL-4 (Fig. 6A – C, respectively). These data indicate a Th1 and Tc1 signature of T cells in brain; there was some evidence of a Th17/Tc17 response, but the increase in $CD4^+$IL-17^+ and $CD8^+$IL-17^+ cells in Aldara-treated mice did not reach significance, likely due to high variability in the data.

Using flow cytometry we assayed microglia and astrocytes for expression of proinflammatory cytokines (TNFα, IL-6 and IFN-γ). Aldara treatment significantly increased the number of microglia producing all 3 cytokines relative to controls (Fig. 6E), and the number of astrocytes producing IL-6

and IFN-γ (Fig 6F). We also observed a significantly increased proinflammatory signature in infiltrating monocytes (producing TNFα and IL-6) in the treated mice (Fig. 6G) (see supplementary methods for our gating strategies). Further analysis of the whole brain transcriptome dataset revealed upregulation of genes for proinflammatory cytokines and chemokines in Aldara-treated mice (Fig. 6H). These chemokines are key to immune cell ingress to brain[38].

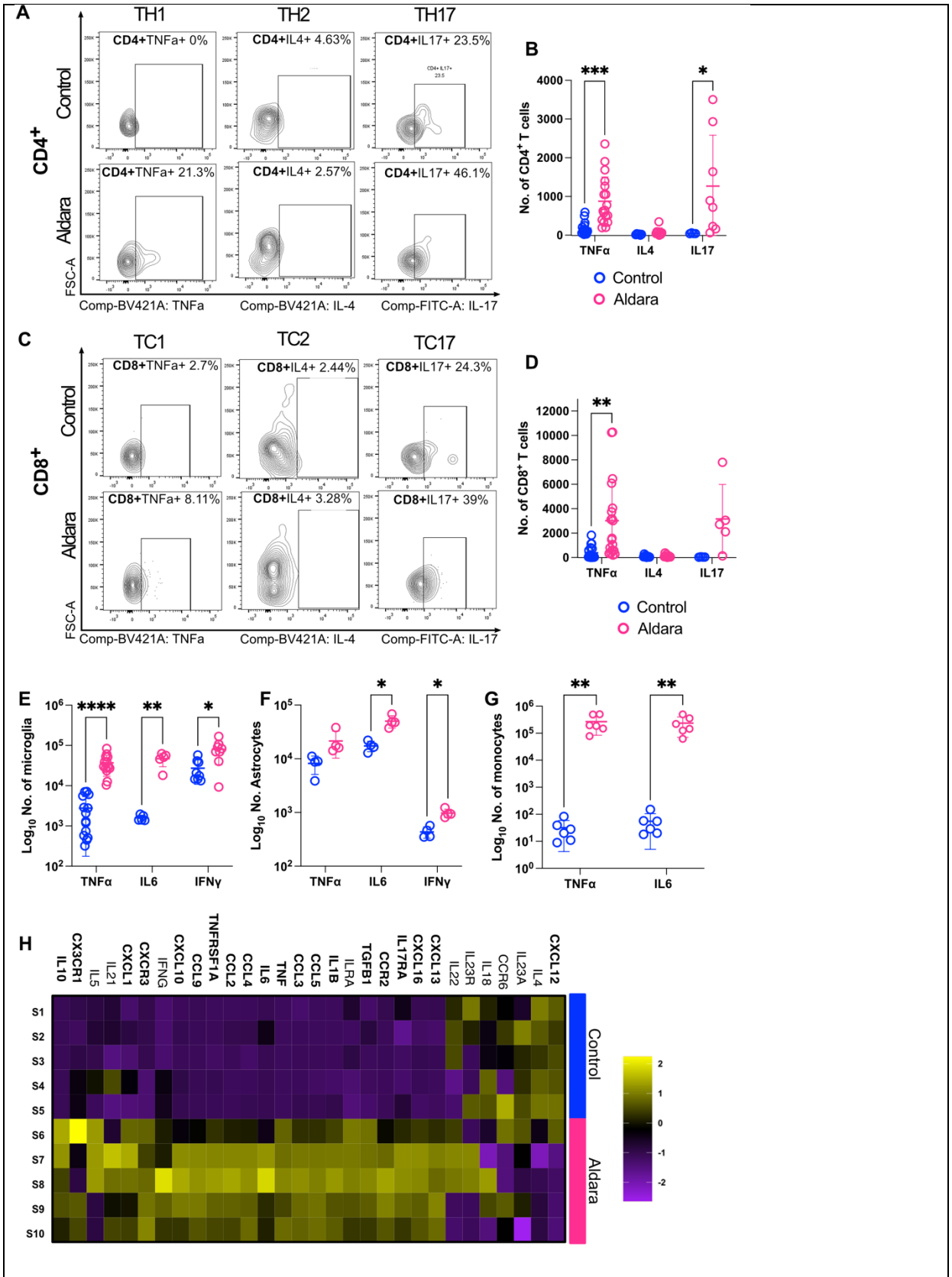

Figure 6: Aldara induces a neuroinflammatory response via multiple cell types. In all panels control mice are shown in blue and Aldara-treated mice in pink. **A&C,** Contour maps showing the numbers of CD4$^+$ (upper two rows) and CD8$^+$ (lower two rows) T cells in brain homogenates from control- and Aldara-treated mice. **B**, Expression of Th1 type cytokine TNFα

and IL17 increases in Aldara-treated brains **but no** change in IL4, a Th2-type cytokine, was observed in $CD4^+$ T cells as compared to control; TNFα n= 174 ± 174 *vs* 876 ± 625, p = 0.0006 , IL-4 n= 20 ± 13 *vs* 88 ± 102 , IL-17 n= 47 ± 11 *vs* 1268 ± 1314.2, as found with *post hoc* Šídák's multiple comparisons test after mixed-effects analysis. **D**, Aldara treatment resulted in an increase in TNFα expression in $CD8^+$ T cells as compared to control. TNFα n= 389 ± 530 *vs* 3022 ± 3183, p = 0.0063, IL-4 n= 99 ± 85 *vs* 130 ± 114, IL17 n= 39 ± 14 *vs* 3127 ± 2827, as found with *post hoc* Šídák's multiple comparisons test after mixed-effects analysis. **E**, Microglia displayed a significant increase in all three cytokines, as compared to control, TNFα n= 2764 ± 2587 *vs* 37010 ± 19800, p = < 0.0001 (TNFα), IL6 n= 1590 ± 265 *vs* 46799 ± 17232, p = 0.0126 (IL6), IFN-γ n= 27259 ± 16448 *vs* 80073 ± 46930, p = 0.0456 as found with *post hoc* Šídák's multiple comparisons test after mixed-effects analysis. **F**, Astrocytes displayed no change in TNFα but a significant increase in IL6 and IFN-γ, TNFα n= 8176 ± 3071 *vs* 21457 ± 11197, IL6 n= 17361 ± 3795 *vs* 50294 ± 12936, p = 0.0334, IFN-γ n= 435 ± 105 *vs* 976 ± 176, p = 0.0102 as found with *post hoc* Šídák's multiple comparisons test after mixed-effects analysis. **G**, Infiltrating peripheral myeloid cells showed a significant increase in TNFα and IL6 expression as compared to control, TNFα n= 32 ± 28 *vs* 267187 ± 183460, p = 0.0025, IL6 n= 55 ± 50 *vs* 235076 ± 164587, p = 0.0071 as found with *post hoc* Šídák's multiple comparisons test after mixed-effects analysis. Data plotted as mean ± SD. . **H**, Searchlight heatmap showing relative whole brain expression levels for a range of cytokines from control- and Aldara-treated mice. Each square on the heatmap represents one mouse (S1 to S10).

Immune mechanisms underlying neuroinflammatory response

To assess the contribution of infiltrating immune cells to the Aldara model phenotype, we used systemic treatment of antibodies to CD4 and CD8 to knock down circulating and thus brain infiltrating T cell populations. To inhibit egress of monocytes from bone marrow into the periphery and subsequent infiltration to the brain, we used iCCRKO mice lacking the chemokine receptors CCR1, CC2, CCR3 and CCR5[39]. Control experiments using flow cytometry demonstrated that, following Aldara treatment, T cell depletion resulted in a substantial knock-down of T cells in blood, brain and spleen (supplementary fig. 4), and in iCCRKO mice there was a substantial reduction in circulating monocytes (supplementary fig. 5). Depletion of CD4/CD8 T cells did not substantially alter the profile of the immune cells seen with Aldara treatment, with the main populations of myeloid, lymphoid and microglia apparent (Fig. 7A). While the T cell depletion affected CD4/CD8 T cells, other ingressing immune cells were unaffected (NK, NKT and B cells).

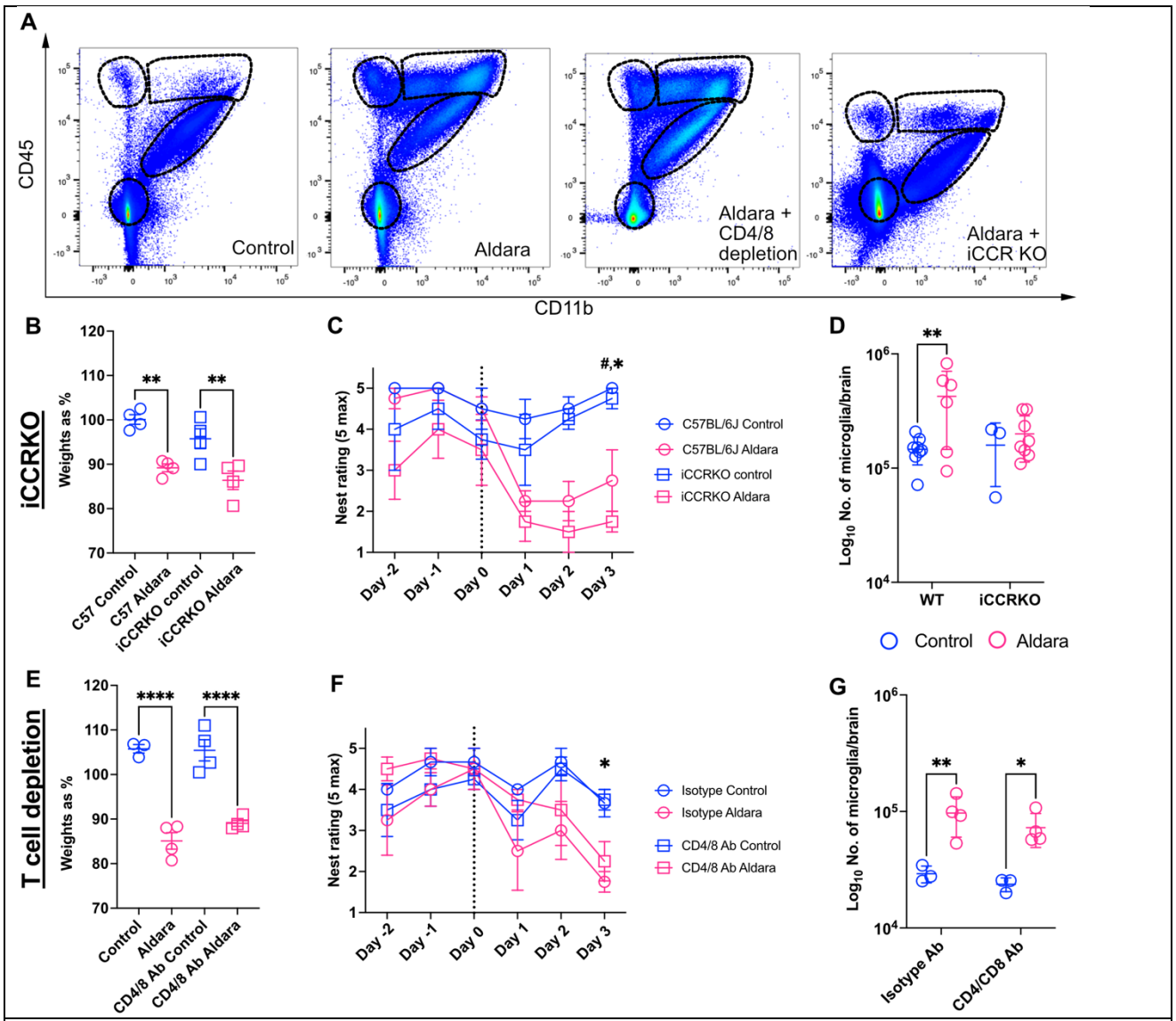

Figure 7: iCCRKO and CD4/CD8 depleted mice retain deficits in nest building and microglial activation in response to 3-day Aldara-treatment. A, Representative basic flow cytometry panels from a single control (**first**), Aldara-treated (**second**), CD4/8 depleted Aldara-treated (third) and iCCRKO Aldara-treated (fourth) experiment. The 4 broad cell types are indicated within dashed lines. **B,** iCCRKO mice experience similar weight loss to wild-type during the 3-day treatment, C57BL6/J control *vs* treated n= 4, 100 ± 2 *vs* 89 ± 2 %, p = 0.0013, iCCRKO control vs treated n= 4, 96 ± 5 *vs* 86 ± 4 %, p = 0.0039, as found with *post hoc* Šídák's multiple comparisons test after one-way ANOVA. **C,** iCCRKO mice show a reduction in nest quality building during the 3-day treatment. C57BL6/J control *vs* treated on cull day n=4 5 ± 0 *vs* 3 ± 2, p = 0.0133, iCCRKO control *vs* treated on cull day 5 ± 1 *vs* 2 ± 1, p = 0.0005, as found with *post hoc* Šídák's multiple comparisons test after two-way ANOVA **D,** iCCRKO mice show a smaller increase in the number of microglial cells as compared to wild-type mice. **E,** CD4/8 depleted mice still show a similar weight loss to wild-type

during the 3-day treatment. Isotype control *vs* treated, n=4, 98 ± 3 *vs* 84 ± 3 %, p < 0.0001, CD4/CD8 Ab control *vs* treated 96 ± 3 *vs* 80 ± 4 %, p < 0.0001, as found with *post hoc* Šídák's multiple comparisons test after one-way ANOVA. **F,** CD4/8 depleted mice show a reduction in nest quality building during the 3-day treatment. Isotype control *vs* treated, n=4, 4 ± 1 *vs* 2 ± 1, p = 0.0013, CD4/CD8 Ab control *vs* treated 4 + 1 *vs* 2+ 1, as found with *post hoc* Šídák's multiple comparisons test after two-way ANOVA. **G** CD4/8 depleted mice show a similar increase in the number of microglial cells as compared to wild-types Isotype control vs treated, n=4, 29199 ± 4806 *vs* 96917 ± 36607 p = 0.0182, CD4/CD8 Ab control *vs* treated 23738 ± 3220 *vs* 72612 ± 23573 p = 0.00927 as found with Tukey's multiple comparison test after two-way ANOVA.

However, Aldara treatment on the iCCRKO mice did show a reduction in the myeloid population after Aldara treatment (Fig 7A), as expected with the majority of the myeloid cell ingress due to monocytes (Fig 5D). We used weight loss and nest-building assays as proxy measures for Aldara-driven deficits in motivational behaviour and neither reducing infiltrating monocytes in iCCRKO mice (Fig. 7B & C) nor blocking CD4/CD8 T cell ingress (Fig. 7E & F) ameliorated these deficits. In the iCCRKO mice, but not in the CD4/CD8 T cell depletion mice, we did see a significant impairment in the Aldara-driven increase in numbers of microglia (or microglia-like) cells (Fig 7D and G, respectively). Interestingly, in the iCCRKO mice, we still observed morphological changes in microglia consistent with a reactive phenotype (supplementary fig. 6).

Further, we sought to determine whether inhibition of the NLRP3 inflammasome could dampen immune responses to Aldara treatment. Astrocytic reactivity in inflammatory states is driven by reactive microglia[40], a process that depends upon activation on the NLRP3 inflammasome in microglia[41–43], signalling via IL-1β. We found that treatment with Aldara significantly increased NLRP3 protein expression in mouse brain (Fig. 8A & B). We employed a brain-penetrant inflammasome inhibitor, NT-0527, to ameliorate the neuroinflammatory response to Aldara. Mice were pre-treated with NT-0527 at 100 mg/kg orally (or vehicle) for 24h before Aldara treatment and then once daily during the Aldara protocol. This treatment was not sufficient to prevent weight loss in response to Aldara treatment (Fig. 8C), but we did observe significant reductions in cytokine production from both microglia (Fig. 8D) and astrocytes (Fig. 8E) after treatment with the NLRP3

inhibitor. Treatment with NT-0527 also blocked Aldara-driven increases in circulating monocytes and neutrophils found in the blood (supplementary figure 8).

Overall, we concluded that reducing infiltration of CD4/CD8 T cells or monocytes could attenuate the immune response to Aldara treatment, as can using an NLRP3 inhibitor as an immune 'circuit breaker' to reduce microglial-driven activation of astrocytes. However, it appears that no single immune mechanism can drive behavioural changes associated with Aldara treatment, perhaps due to the direct actions of imiquimod in the CNS.

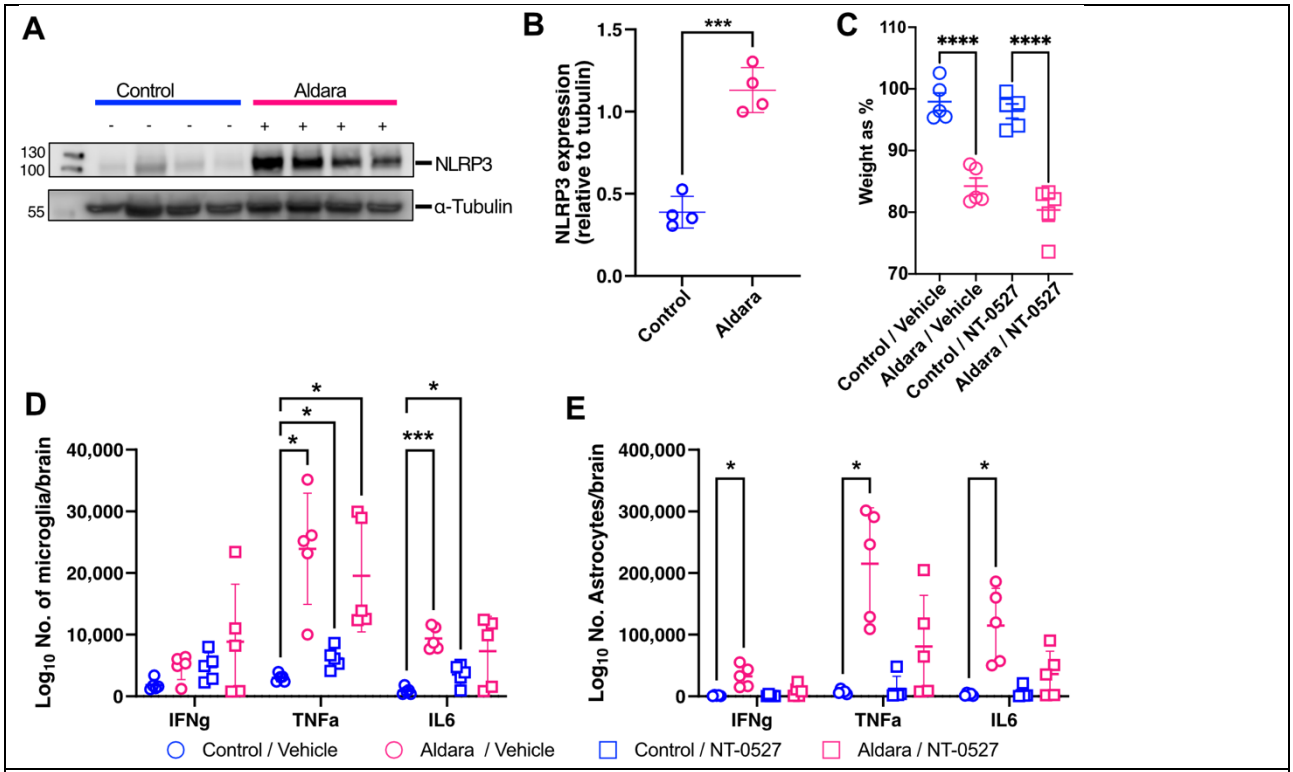

Figure 8: Blocking inflammasome alters the cytokine profile of brain resident cells. A, Western blot shows an increase in the NLRP3 in the brain **in** Aldara treated group as compared to control. **B,** quantification of blot in A. Relative to expression levels of tubulin, NLPR3 expression increased from 0.39 ± 0.1 to 1.13 ± 0.14 after Aldara treatment (n=4 in each group; $p < 0.001$, Student's t test). **C,** NT-0527-treated Aldara mice experience similar weight loss to vehicle-treated Aldara mice; control vehicle vs treated vehicle, n=5, 98 ± 3 *vs* 84 ± 3% $p < 0.0001$, control NT-0527 vs Aldara treated NT-0527, n=5, 96 ± 3 *vs* 80 ± 4%, $p < 0.0001$, as found with *post hoc* Šídák's multiple comparisons test after two-way ANOVA. **D,** Number of microglia, expressing IL-6, but not TNFα and IFN-γ, is reduced in Aldara-treated animals treated with NLRP3 antagonist, as seen with flow cytometry, n=5. ***TNFα***: control / vehicle: 2998 ± 649; Aldara / Vehicle, 23931 ± 9029; control / NT-0527, 6163 ± 1689; Aldara / NT-0527, 19534 ± 9074. ***IL-6***: Control / Vehicle,875 ± 582; Aldara / Vehicle, 9397 ± 1876; control / NT-0527, 3550 ± 1658; Aldara / NT-0527, 3550 ± 1658. ***IFN-γ***: control / vehicle, 1828 ± 897; Aldara / vehicle,

4780 ± 2067; control / NT-0527 4740 ± 2320; Aldara / NT-0527, 8859 ± 9317. All statistical comparisons *vs* control / vehicle; *post hoc* Šídák's multiple comparisons test after two-way ANOVA. **E,** Number of astrocytes, expressing IFN-γ, TNFα and IL-6, is reduced in Aldara-treated animals treated with NLRP3 antagonist, as seen with flow cytometry, n=5. ***TNFα:*** control / vehicle, 7245 ± 3343; Aldara / vehicle, 215313 ± 90628; control / NT-0527, 12075 ± 20288; Aldara / NT-0527, 80809 ± 8290. ***IL-6***: control / vehicle, 2803 ± 2079; Aldara / vehicle 114687 ± 60531; control / NT-0527, 5205 ± 8883; Aldara / NT-0527, 36195 ± 37113. ***IFN-γ:*** control / vehicle, 1181 ± 882; Aldara / vehicle, 32601 ± 17405; control / NT-0527, 1083 ± 1521; Aldara / NT-0527, 8859 ± 9317 p=0.3698. All statistical comparisons *vs* control / vehicle; *post hoc* Šídák's multiple comparisons test after two-way ANOVA.

Discussion

The aim of our study was elucidation of the link between neuroinflammation and depression-like behaviours. We took a multi-scale approach to characterise the neurobiological changes occurring due to Aldara-driven neuroinflammation at the protein, cellular and synaptic levels. We observed robust changes in immune activation, infiltration of leukocytes into the brain, including CD4+ T cells into the brain parenchyma and glial reactivity. Behavioural changes, including reduced sucrose preference and impaired nest-building, were consistent with an anhedonia-like state in mice[44]. In humans with PsD, increased connectivity between thalamus and ventral striatum was associated with higher depression scores, and our mouse model also displayed alterations in thalamostriatal signalling. Communication between striatum, thalamus and cortical regions are key to motivational behaviour[45] . Mice appeared to have normal locomotor function in open field and rotarod tests but displayed a 'stop-start' behaviour during EPM, which is consistent with a reduced intrinsic motivation to carry out exploratory behaviours. Our data fit with the existing literature that show other forms of neuroinflammation can induce depression-like behaviours[12,46] and adds to the construct validity of Aldara as a model for inflammation-induced depression seen in humans[1,3].

Neurobiological changes in reward circuitry

A recent study reported higher connectivity between thalamus and ventral striatum in individuals with anhedonia[34], and our study in PsD patients replicated this, suggesting inflammation-driven and

idiopathic anhedonia could converge on common neural mechanisms. We saw a trend towards higher thalamic activation in human depression, and the robust c-Fos expression in mouse within hours of Aldara application further implicates midline thalamus as a key region in inflammation-driven depression or impaired reward-related behaviours across species. After 3 days of Aldara treatment, we found that the evoked thalamic AMPA receptor-mediated EPSC onto ventral MSNs was substantially weaker compared to control-treated mice, but with no change to the AMPA/NMDA ratio nor change in the frequency of amplitude of spontaneous EPSPs. The lack of change in AMPA/NMDA ratio would suggest the change in amplitude of the thalamic input is not a result of synaptic plasticity such as LTD[47,48].

Our interpretation of the data is that increased midline thalamic activity initially results in excessive excitatory transmission. The precise mechanism through which Aldara treatment rapidly drives excitation in midline thalamus is unclear, but some data from a recent sheep study suggests TLR7 receptors may be present directly on thalamic neurons[49]. Inflammation decreases astrocytic clearance and buffering of glutamate by downregulation of glutamate transporters[50], which may have exacerbated this effect. Our observed downregulation of the astrocytic glutamate transporter *EAAT2/SLC1A2* transcript is consistent with this. Only 5% of striatal neurons are inhibitory interneurons[51], far fewer than in cortex or hippocampus, so the lack of recurrent inhibition may make this region particularly vulnerable to excess glutamate. Indeed, Aldara treatment led to increased VGlut2-containing terminals in striatum but not cortex, with no change in VGlut1 immunolabelling, implying a specific alteration in the thalamostriatal pathway. We suggest that increased excitatory signalling leads to AMPA receptor internalisation in ventral MSNs. This is supported at the transcript level by reductions in Homer1, which is involved in AMPA receptor homeostatic scaling[36], as well as downregulation of glutamate-gated ion channels[29] .

Immune mechanisms underlying neuroinflammatory response

The mechanism of Aldara-driven neuroinflammation included cytokine release from both infiltrating immune and resident glial cells. Reactive microglia showed increased expression of macrophage-

like markers: MHCII, F4/80 and MSR1. While previous data indicate that microglia can proliferate in response to inflammation [52], the apparent increase we seen post Aldara might be attributable to such proliferation, to differentiation of ingressing monocytes, or to perivascular macrophages. The absence of an increase, despite presence of reactivity, in the iCCRKO-mouse line could implicate the latter given their CCR2-dependent turnover. Immunohistochemistry revealed no morphological changes associated with astrocytes, using GFAP as a marker, yet a triple positive marker approach to quantify reactive astrocytes with GFAP, S100β and ASCA2 via flow cytometry markers found these astrocytes significantly increased production of the proinflammatory cytokines IL-6 and IFN-γ. Given that the triple-positive subset of astrocytes that produced the proinflammatory cytokines constituted roughly a third of all S100β^{+ve} and ACSA^{+ve} astrocytes, we conclude that to see a morphological change a different immunofluorescent staining strategy was required. Reactive microglia can induce reactivity in astrocytes via secretion of IL1α, TNFα, and C1q[40], and subsets of reactive astrocytes can be defined by interferon-responsive genes such as *Igtp*, *Mx1* and *Ifit3*[53]. We found these genes to be significantly upregulated in treated *vs* control brains (see supplementary material).

We found both CD4$^+$ and CD8$^+$ T cells throughout the brain parenchyma of Aldara-treated mice. Neuroinflammation is associated with a characteristic T cell signature in the brain[54] and, while depletion of T cells was successful in our model, mice still displayed weight loss and deficits in nest-building after Aldara treatment. Recent studies have linked recruitment of peripheral monocytes into the brain with deficits in behaviour associated with inflammation[55]. In one study, cognitive impairments and neurite remodelling was attributable solely to circulating CX3CR1+ monocyte-derived TNFα[13], but blocking monocyte ingress in our model had no effect on nest-building. Activation of the NLPR3 inflammasome in microglia appears to be a key step for amplifying immune signals in the brain[41–43] and NLPR3 has been posited as an important target in inflammation-driven depression[19,56,57]. We used a brain-penetrant NLRP3 inflammasome inhibitor in the Aldara model and, while significantly reducing cytokine production in both microglia and astrocytes, this approach was not sufficient to prevent weight loss associated with the model. No single pathway targeted in our interventions was necessary for the development of behavioural deficits seen in Aldara, which is

likely due to the model acting via both central and peripheral mechanisms, and engaging such a strong immune response.

Limitations to the model

We have previously demonstrated that imiquimod enters the brain and directly drives neuroinflammation via activation of TLR7. However, IMQ (especially when formulated with isostearic acid in Aldara cream) can also cause a peripheral inflammatory response by driving a psoriasis-like skin inflammation[58]. As such, the neuroinflammatory response has two potential drivers: the direct effects of IMQ on the brain and the effects of peripheral inflammation via neural and humoral routes, and these two may act synergistically [58]. It is not possible in this study to separate these two different inflammatory pathways. However, we do not believe that this is a significant confounding factor for interpreting our results, given that most humans experiencing psychiatric symptoms due to inflammatory disease will likely experience both central and peripheral inflammation.

Conclusions

We can conclude that in our model of neuroinflammation, the overall pro-inflammatory milieu is driven by both ingressing cells (T cells and monocytes) and resident cells (astrocytes and microglia). These inflammation-driven changes ultimately lead to an anhedonic phenotype, which cannot be rescued by removing one of the factors at play, suggesting a synergistic interplay between all cellular compartments. We found that anhedonia-like or depressive symptoms occurring with neuroinflammation is associated with perturbed thalamostriatial signalling in both humans and mice. This circuit, and the immune mechanisms revealed in our study, present attractive targets for developing new anti-depressant therapies in at least the subset of depressed individuals showing heightened inflammation.

Acknowledgements

We gratefully acknowledge the support of the Inger and George M Simpson Biological Psychiatry Scholarships. This work was supported by PhD studentships from the Saudi Arabia Ministry of

Science (HAF) and the Government of Turkey (YK). The authors gratefully acknowledge the Glasgow Imaging Facility for their support and assurance in this work. The authors gratefully acknowledge the Flow Core Facility of the University of Glasgow for their support & assistance in this work. For the purpose of open access, the authors have applied a Creative Commons Attribution (CC-BY) licence to any Author Accepted Manuscript version arising from this submission.

Conflict of interests

Peter Thornton is an employee and equity holder of NodThera. All other authors declare that they have no conflicts of interest.

References

1. Nerurkar, L., Siebert, S., McInnes, I.B., and Cavanagh, J. (2019). Rheumatoid arthritis and depression: an inflammatory perspective. Lancet Psychiatry *6*, 164–173. https://doi.org/10.1016/s2215-0366(18)30255-4.

2. Luna, P.C., Chu, C.-Y., Fatani, M., Borlenghi, C., Adora, A., Llamado, L.Q., and Wee, J. (2023). Psychosocial Burden of Psoriasis: A Systematic Literature Review of Depression Among Patients with Psoriasis. Dermatol. Ther. *13*, 3043–3055. https://doi.org/10.1007/s13555-023-01060-5.

3. Brock, J., Basu, N., Schlachetzki, J.C.M., Schett, G., McInnes, I.B., and Cavanagh, J. (2023). Immune mechanisms of depression in rheumatoid arthritis. Nat. Rev. Rheumatol. *19*, 790–804. https://doi.org/10.1038/s41584-023-01037-w.

4. Yang, C., Wardenaar, K.J., Bosker, F.J., Li, J., and Schoevers, R.A. (2019). Inflammatory markers and treatment outcome in treatment resistant depression: A systematic review. J. Affect. Disord. *257*, 640–649. https://doi.org/10.1016/j.jad.2019.07.045.

5. Levey, D.F., Stein, M.B., Wendt, F.R., Pathak, G.A., Zhou, H., Aslan, M., Quaden, R., Harrington, K.M., Nuñez, Y.Z., Overstreet, C., et al. (2021). Bi-ancestral depression GWAS in the Million Veteran Program and meta-analysis in >1.2 million individuals highlight new therapeutic directions. Nat. Neurosci. *24*, 954–963. https://doi.org/10.1038/s41593-021-00860-2.

6. Chiu, W.-C., Su, Y.-P., Su, K.-P., and Chen, P.-C. (2017). Recurrence of depressive disorders after interferon-induced depression. Transl. Psychiatry *7*, e1026–e1026. https://doi.org/10.1038/tp.2016.274.

7. Kappelmann, N., Arloth, J., Georgakis, M.K., Czamara, D., Rost, N., Ligthart, S., Khandaker, G.M., and Binder, E.B. (2021). Dissecting the Association Between Inflammation, Metabolic Dysregulation, and Specific Depressive Symptoms. JAMA Psychiatry *78*, 161–170. https://doi.org/10.1001/jamapsychiatry.2020.3436.

8. Dipasquale, O., Cooper, E.A., Tibble, J., Voon, V., Baglio, F., Baselli, G., Cercignani, M., and Harrison, N.A. (2016). Interferon-α acutely impairs whole-brain functional connectivity network architecture – A preliminary study. Brain, Behav., Immun. *58*, 31–39. https://doi.org/10.1016/j.bbi.2015.12.011.

9. Davies, K.A., Cooper, E., Voon, V., Tibble, J., Cercignani, M., and Harrison, N.A. (2021). Interferon and anti-TNF therapies differentially modulate amygdala reactivity which predicts associated bidirectional changes in depressive symptoms. Mol. Psychiatry *26*, 5150–5160. https://doi.org/10.1038/s41380-020-0790-9.

10. Martins, D., Dipasquale, O., Davies, K., Cooper, E., Tibble, J., Veronese, M., Frigo, M., Williams, S.C.R., Turkheimer, F., Cercignani, M., et al. (2022). Transcriptomic and cellular decoding of functional brain connectivity changes reveal regional brain vulnerability to pro- and anti-inflammatory therapies. Brain, Behav., Immun. *102*, 312–323. https://doi.org/10.1016/j.bbi.2022.03.004.

11. Grippo, A.J., Francis, J., Beltz, T.G., Felder, R.B., and Johnson, A.K. (2005). Neuroendocrine and cytokine profile of chronic mild stress-induced anhedonia. Physiol. Behav. *84*, 697–706. https://doi.org/10.1016/j.physbeh.2005.02.011.

12. Yin, R., Zhang, K., Li, Y., Tang, Z., Zheng, R., Ma, Y., Chen, Z., Lei, N., Xiong, L., Guo, P., et al. (2023). Lipopolysaccharide-induced depression-like model in mice: meta-analysis and systematic evaluation. Front. Immunol. *14*, 1181973. https://doi.org/10.3389/fimmu.2023.1181973.

13. Garré, J.M., Silva, H.M., Lafaille, J.J., and Yang, G. (2017). CX3CR1+ monocytes modulate learning and learning-dependent dendritic spine remodeling via TNF-α. Nat Med *23*, 714–722. https://doi.org/10.1038/nm.4340.

14. Stellwagen, D., and Malenka, R.C. (2006). Synaptic scaling mediated by glial TNF-α. Nature *440*, 1054–1059. https://doi.org/10.1038/nature04671.

15. Santello, M., Bezzi, P., and Volterra, A. (2011). TNFα Controls Glutamatergic Gliotransmission in the Hippocampal Dentate Gyrus. Neuron *69*, 988–1001. https://doi.org/10.1016/j.neuron.2011.02.003.

16. Haji, N., Mandolesi, G., Gentile, A., Sacchetti, L., Fresegna, D., Rossi, S., Musella, A., Sepman, H., Motta, C., Studer, V., et al. (2012). TNF-α-mediated anxiety in a mouse model of multiple sclerosis. Exp. Neurol. *237*, 296–303. https://doi.org/10.1016/j.expneurol.2012.07.010.

17. Lewitus, G.M., Pribiag, H., Duseja, R., St-Hilaire, M., and Stellwagen, D. (2014). An Adaptive Role of TNFα in the Regulation of Striatal Synapses. J. Neurosci. *34*, 6146–6155. https://doi.org/10.1523/jneurosci.3481-13.2014.

18. Stellwagen, D., Beattie, E.C., Seo, J.Y., and Malenka, R.C. (2005). Differential Regulation of AMPA Receptor and GABA Receptor Trafficking by Tumor Necrosis Factor-α. J. Neurosci. *25*, 3219–3228. https://doi.org/10.1523/jneurosci.4486-04.2005.

19. Kaufmann, F.N., Costa, A.P., Ghisleni, G., Diaz, A.P., Rodrigues, A.L.S., Peluffo, H., and Kaster, M.P. (2017). NLRP3 inflammasome-driven pathways in depression: Clinical and preclinical findings. Brain Behav Immun *64*, 367–383. https://doi.org/10.1016/j.bbi.2017.03.002.

20. Nerurkar, L., McColl, A., Graham, G., and Cavanagh, J. (2017). The Systemic Response to Topical Aldara Treatment is Mediated Through Direct TLR7 Stimulation as Imiquimod Enters the Circulation. Sci. Rep. *7*, 16570. https://doi.org/10.1038/s41598-017-16707-5.

21. McColl, A., Thomson, C.A., Nerurkar, L., Graham, G.J., and Cavanagh, J. (2016). TLR7-mediated skin inflammation remotely triggers chemokine expression and leukocyte accumulation in the brain. J. Neuroinflammation *13*, 102. https://doi.org/10.1186/s12974-016-0562-2.

22. Faul, F., Erdfelder, E., Lang, A.-G., and Buchner, A. (2007). G*Power 3: A flexible statistical power analysis program for the social, behavioral, and biomedical sciences. Behav Res Methods *39*, 175–191. https://doi.org/10.3758/bf03193146.

23. Deacon, R.M. (2006). Assessing nest building in mice. Nat. Protoc. *1*, 1117–1119. https://doi.org/10.1038/nprot.2006.170.

24. Nieto-Castanon, A. (2020). Handbook of functional connectivity Magnetic Resonance Imaging methods in CONN. 63–82. https://doi.org/10.56441/hilbertpress.2207.6602.

25. Yang, H., Long, X.-Y., Yang, Y., Yan, H., Zhu, C.-Z., Zhou, X.-P., Zang, Y.-F., and Gong, Q.-Y. (2007). Amplitude of low frequency fluctuation within visual areas revealed by resting-state functional MRI. NeuroImage *36*, 144–152. https://doi.org/10.1016/j.neuroimage.2007.01.054.

26. Berendse, H.W., and Groenewegen, H.J. (1990). Organization of the thalamostriatal projections in the rat, with special emphasis on the ventral striatum. J. Comp. Neurol. *299*, 187–228. https://doi.org/10.1002/cne.902990206.

27. Schindelin, J., Arganda-Carreras, I., Frise, E., Kaynig, V., Longair, M., Pietzsch, T., Preibisch, S., Rueden, C., Saalfeld, S., Schmid, B., et al. (2012). Fiji: an open-source platform for biological-image analysis. Nat Methods *9*, 676–682. https://doi.org/10.1038/nmeth.2019.

28. Arzt, M., Deschamps, J., Schmied, C., Pietzsch, T., Schmidt, D., Tomancak, P., Haase, R., and Jug, F. (2022). LABKIT: Labeling and Segmentation Toolkit for Big Image Data. Front. Comput. Sci. *4*. https://doi.org/10.3389/fcomp.2022.777728.

29. Gardner-Stephen, K., Carvajal-Quisilema, R.J., Andrianova, L., McGonigal, R., Sharma, D., Barrie, J.A., Saathoff, M., Cole, J.J., Jamieson, N.B., Craig, M.T., et al. (2025). Neuroinflammation driven by TLR7 activation in mice results in a global inflammatory response driving circuit-specific changes in neuronal gene expression. bioRxiv, 2025.04.25.650583. https://doi.org/10.1101/2025.04.25.650583.

30. Love, M.I., Huber, W., and Anders, S. (2014). Moderated estimation of fold change and dispersion for RNA-seq data with DESeq2. Genome Biol. *15*, 550. https://doi.org/10.1186/s13059-014-0550-8.

31. Cole, J.J., Faydaci, B.A., McGuinness, D., Shaw, R., Maciewicz, R.A., Robertson, N.A., and Goodyear, C.S. (2021). Searchlight: automated bulk RNA-seq exploration and visualisation using dynamically generated R scripts. BMC Bioinform. *22*, 411. https://doi.org/10.1186/s12859-021-04321-2.

32. Heshmati, M., and Russo, S.J. (2015). Anhedonia and the Brain Reward Circuitry in Depression. Curr. Behav. Neurosci. Rep. *2*, 146–153. https://doi.org/10.1007/s40473-015-0044-3.

33. Fremeau, R.T., Troyer, M.D., Pahner, I., Nygaard, G.O., Tran, C.H., Reimer, R.J., Bellocchio, E.E., Fortin, D., Storm-Mathisen, J., and Edwards, R.H. (2001). The Expression of Vesicular Glutamate Transporters Defines Two Classes of Excitatory Synapse. Neuron *31*, 247–260. https://doi.org/10.1016/s0896-6273(01)00344-0.

34. Leonard, B.T., Kark, S.M., Granger, S.J., Adams, J.G., McMillan, L., and Yassa, M.A. (2024). Anhedonia is associated with higher functional connectivity between the nucleus accumbens and paraventricular nucleus of thalamus. J. Affect. Disord. *366*, 1–7. https://doi.org/10.1016/j.jad.2024.08.113.

35. Klapoetke, N.C., Murata, Y., Kim, S.S., Pulver, S.R., Birdsey-Benson, A., Cho, Y.K., Morimoto, T.K., Chuong, A.S., Carpenter, E.J., Tian, Z., et al. (2014). Independent optical excitation of distinct neural populations. Nat Methods *11*, 338–346. https://doi.org/10.1038/nmeth.2836.

36. Clifton, N.E., Trent, S., Thomas, K.L., and Hall, J. (2019). Regulation and Function of Activity-Dependent Homer in Synaptic Plasticity. Mol. Neuropsychiatry *5*, 147–161. https://doi.org/10.1159/000500267.

37. Korin, B., Ben-Shaanan, T.L., Schiller, M., Dubovik, T., Azulay-Debby, H., Boshnak, N.T., Koren, T., and Rolls, A. (2017). High-dimensional, single-cell characterization of the brain's immune compartment. Nat. Neurosci. *20*, 1300–1309. https://doi.org/10.1038/nn.4610.

38. Ransohoff, R.M., Glabinski, A., and Tani, M. (1996). Chemokines in immune-mediated inflammation of the central nervous system. Cytokine Growth Factor Rev. *7*, 35–46. https://doi.org/10.1016/1359-6101(96)00003-2.

39. Dyer, D.P., Medina-Ruiz, L., Bartolini, R., Schuette, F., Hughes, C.E., Pallas, K., Vidler, F., Macleod, M.K.L., Kelly, C.J., Lee, K.M., et al. (2019). Chemokine Receptor Redundancy and Specificity Are Context Dependent. Immunity *50*, 378-389.e5. https://doi.org/10.1016/j.immuni.2019.01.009.

40. Liddelow, S.A., Guttenplan, K.A., Clarke, L.E., Bennett, F.C., Bohlen, C.J., Schirmer, L., Bennett, M.L., Münch, A.E., Chung, W.-S., Peterson, T.C., et al. (2017). Neurotoxic reactive astrocytes are induced by activated microglia. Nature *541*, 481–487. https://doi.org/10.1038/nature21029.

41. Riester, K., Brawek, B., Savitska, D., Fröhlich, N., Zirdum, E., Mojtahedi, N., Heneka, M.T., and Garaschuk, O. (2020). In vivo characterization of functional states of cortical microglia during peripheral inflammation. Brain, Behav., Immun. *87*, 243–255. https://doi.org/10.1016/j.bbi.2019.12.007.

42. Li, S., Fang, Y., Zhang, Y., Song, M., Zhang, X., Ding, X., Yao, H., Chen, M., Sun, Y., Ding, J., et al. (2022). Microglial NLRP3 inflammasome activates neurotoxic astrocytes in depression-like mice. Cell Rep. *41*, 111532. https://doi.org/10.1016/j.celrep.2022.111532.

43. Tejera, D., Mercan, D., Sanchez-Caro, J.M., Hanan, M., Greenberg, D., Soreq, H., Latz, E., Golenbock, D., and Heneka, M.T. (2019). Systemic inflammation impairs microglial Aβ clearance through NLRP3 inflammasome. EMBO J. *38*, EMBJ2018101064. https://doi.org/10.15252/embj.2018101064.

44. Scheggi, S., Montis, M.G.D., and Gambarana, C. (2018). Making Sense of Rodent Models of Anhedonia. Int. J. Neuropsychopharmacol. *21*, 1049–1065. https://doi.org/10.1093/ijnp/pyy083.

45. Haber, S.N., and Calzavara, R. (2009). The cortico-basal ganglia integrative network: The role of the thalamus. Brain Res. Bull. *78*, 69–74. https://doi.org/10.1016/j.brainresbull.2008.09.013.

46. Ma, L., Demin, K.A., Kolesnikova, T.O., Kharsko, S.L., Zhu, X., Yuan, X., Song, C., Meshalkina, D.A., Leonard, B.E., Tian, L., et al. (2017). Animal inflammation-based models of depression and their application to drug discovery. Expert Opin. Drug Discov. *12*, 995–1009. https://doi.org/10.1080/17460441.2017.1362385.

47. Citri, A., and Malenka, R.C. (2008). Synaptic Plasticity: Multiple Forms, Functions, and Mechanisms. Neuropsychopharmacology *33*, 18–41. https://doi.org/10.1038/sj.npp.1301559.

48. Ungless, M.A., Whistler, J.L., Malenka, R.C., and Bonci, A. (2001). Single cocaine exposure in vivo induces long-term potentiation in dopamine neurons. Nature *411*, 583–587. https://doi.org/10.1038/35079077.

49. Cho, K.H.T., Wassink, G., Galinsky, R., Xu, B., Mathai, S., Dhillon, S.K., Heuij, L.G. van den, Davidson, J.O., Weaver-Mikaere, L., Bennet, L., et al. (2019). Protective effects of delayed intraventricular TLR7 agonist administration on cerebral white and gray matter following asphyxia in the preterm fetal sheep. Sci. Rep. *9*, 9562. https://doi.org/10.1038/s41598-019-45872-y.

50. Volterra, A., and Meldolesi, J. (2005). Astrocytes, from brain glue to communication elements: the revolution continues. Nat. Rev. Neurosci. *6*, 626–640. https://doi.org/10.1038/nrn1722.

51. Gittis, A.H., and Kreitzer, A.C. (2012). Striatal microcircuitry and movement disorders. Trends Neurosci. *35*, 557–564. https://doi.org/10.1016/j.tins.2012.06.008.

52. Askew, K., Li, K., Olmos-Alonso, A., Garcia-Moreno, F., Liang, Y., Richardson, P., Tipton, T., Chapman, M.A., Riecken, K., Beccari, S., et al. (2017). Coupled Proliferation and Apoptosis Maintain the Rapid Turnover of Microglia in the Adult Brain. Cell Rep. *18*, 391–405. https://doi.org/10.1016/j.celrep.2016.12.041.

53. Prakash, P., Erdjument-Bromage, H., O'Dea, M.R., Munson, C.N., Labib, D., Fossati, V., Neubert, T.A., and Liddelow, S.A. (2024). Proteomic profiling of interferon-responsive reactive astrocytes in rodent and human. Glia *72*, 625–642. https://doi.org/10.1002/glia.24494.

54. Cipollini, V., Anrather, J., Orzi, F., and Iadecola, C. (2019). Th17 and Cognitive Impairment: Possible Mechanisms of Action. Front. Neuroanat. *13*, 95. https://doi.org/10.3389/fnana.2019.00095.

55. Wohleb, E.S., McKim, D.B., Sheridan, J.F., and Godbout, J.P. (2015). Monocyte trafficking to the brain with stress and inflammation: a novel axis of immune-to-brain communication that influences mood and behavior. Front. Neurosci. *8*, 447. https://doi.org/10.3389/fnins.2014.00447.

56. Roy, S., Ansari, M.A., Choudhary, K., and Singh, S. (2023). NLRP3 inflammasome in depression: A review. Int. Immunopharmacol. *117*, 109916. https://doi.org/10.1016/j.intimp.2023.109916.

57. Iwata, M., Ota, K.T., and Duman, R.S. (2013). The inflammasome: Pathways linking psychological stress, depression, and systemic illnesses. Brain, Behav., Immun. *31*, 105–114. https://doi.org/10.1016/j.bbi.2012.12.008.

58. Straß, S., Geiger, J., Martorelli, M., Geiger, S., Cloos, N., Keppler, M., Fischer, T., Riexinger, L., Schwamborn, A., Guezguez, J., et al. (2023). Isostearic acid is an active component of imiquimod formulations used to induce psoriaform disease models. Inflammopharmacology *31*, 799–812. https://doi.org/10.1007/s10787-023-01175-3.